Chapter 7 Precision Measurements with a High-Intensity Neutrino Beam

The LBNE near neutrino detector provides scientific value beyond its essential role of calibrating beam and neutrino interaction properties for the long-baseline physics program described in Chapter 4. By virtue of the theoretically clean, purely weak leptonic processes involved, neutrino beams have historically served as unique probes for new physics in their interactions with matter. The high intensity and broad energy range of the LBNE beam will open the door for a highly capable near detector to perform its own diverse program of incisive investigations.

The reduction of systematic uncertainties for the neutrino oscillation program requires excellent resolution in the reconstruction of neutrino events. Combined with the unprecedented neutrino fluxes available — which will allow the collection of $\mathcal{O}(10^8)$ inclusive neutrino charged current (CC) interactions for 10^{22} protons-on-target (POT) just downstream of the beamline — the near detector (ND) will significantly enhance the LBNE long-baseline oscillation program and produce a range of short-baseline neutrino scattering physics measurements. The combined statistics and resolution expected in the ND will allow precise tests of fundamental interactions resulting in a better understanding of the structure of matter.

Table 7.1 lists the expected number of beam-neutrino interactions per ton of detector at the LBNE ND site, located 459 m downstream from the target.

This chapter presents a short description of some of the studies that can be performed with LBNE's fine-grained near neutrino detector and gives a flavor of the outstanding physics potential. A more detailed and complete discussion of the ND physics potential can be found in [1].

Appendix B describes neutrino scattering kinematics and includes definitions of the kinematic variables used in this chapter.

7.1 Precision Measurements with Long-Baseline Oscillations

From the studies of uncertainties and the impact of the spectral shape presented in Section 4.3.2, it is evident that to fully realize the goals of the full LBNE scientific program — in particular, sensitivity to CP violation and the precision measurement of the three-flavor oscillation parameters — it is necessary to characterize the expected unoscillated neutrino flux with high precision. In addition to the precise determination of the neutrino flux, shape and flavor composition, the char-

Table 7.1: Estimated interaction rates in the neutrino (second column) and antineutrino (third column) beams per ton of detector (water) for 1×10^{20} POT at 459 m assuming neutrino cross-section predictions from NUANCE [2] and a 120-GeV proton beam using the CDR reference design. Processes are defined at the initial neutrino interaction vertex and thus do not include final-state effects. These estimates do not include detector efficiencies or acceptance [3,4].

Production mode	ν_μ Events	$\overline{\nu}_\mu$ Events
CC QE ($\nu_\mu n \to \mu^- p$)	50,100	26,300
NC elastic ($\nu_\mu N \to \nu_\mu N$)	18,800	8,980
CC resonant π^+ ($\nu_\mu N \to \mu^- N \pi^+$)	67,800	0
CC resonant π^- ($\overline{\nu}_\mu N \to \mu^+ N \pi^-$)	0	20,760
CC resonant π^0 ($\nu_\mu n \to \mu^- \, p \, \pi^0$)	16,200	6,700
NC resonant π^0 ($\nu_\mu N \to \nu_\mu \, N \, \pi^0$)	16,300	7,130
NC resonant π^+ ($\nu_\mu p \to \nu_\mu \, n \, \pi^+$)	6,930	3,200
NC resonant π^- ($\nu_\mu n \to \nu_\mu \, p \, \pi^-$)	5,980	2,570
CC DIS ($\nu_\mu N \to \mu^- X$ or $\overline{\nu}_\mu N \to \mu^+ X$, $W > 2$)	66,800	13,470
NC DIS ($\nu_\mu N \to \nu_\mu X$ or $\overline{\nu}_\mu N \to \overline{\nu}_\mu X$, $W > 2$)	24,100	5,560
NC coherent π^0 ($\nu_\mu A \to \nu_\mu A \pi^0$ or $\overline{\nu}_\mu A \to \overline{\nu}_\mu A \pi^0$)	2,040	1,530
CC coherent π^+ ($\nu_\mu A \to \mu^- A \pi^+$)	3,920	0
CC coherent π^- ($\overline{\nu}_\mu A \to \mu^+ A \pi^-$)	0	2,900
NC resonant radiative decay ($N^* \to N\gamma$)	110	50
NC elastic electron ($\nu_\mu e^- \to \nu_\mu e^-$ or $\overline{\nu}_\mu e^- \to \overline{\nu_\mu} e^-$)	30	17
Inverse Muon Decay ($\nu_\mu e \to \mu^- \nu_e$)	12	0
Other	42,600	15,800
Total CC (rounded)	**236,000**	**81,000**
Total NC+CC (rounded)	**322,000**	**115,000**

acterization of different neutrino interactions and interaction cross sections on a liquid argon target is necessary to estimate physics backgrounds to the oscillation measurements. The high-resolution near tracking detector described in Section 3.5 can measure the unoscillated flux normalization, shape and flavor to a few percent using systematically independent techniques that are discussed in the following sections.

7.1.1 Determination of the Relative Neutrino and Antineutrino Flux

The most promising method of determining the shape of the ν_μ and $\overline{\nu}_\mu$ flux is by measuring CC events with low hadronic-energy deposition (low-ν) where ν is the total energy of the hadrons that are produced after a neutrino interaction, $E_\nu - E_\mu$. It is important to note that not all the hadrons escape the remnant nucleus, and intranuclear effects will smear the visible energy of the hadronic system. A method of relative flux determination known as low-ν_0 — where ν_0 is a given value of visible hadronic energy in the interaction that is selected to minimize the fraction of the total interaction energy carried by the hadronic system — is well developed [5]. The method follows from the general expression of the ν-nucleon differential cross section:

$$\mathcal{N}(\nu < \nu_0) \simeq C\Phi(E_\nu)\nu_0 \left[\mathcal{A} + \left(\frac{\nu_0}{E_\nu}\right)\mathcal{B} + \left(\frac{\nu_0}{E_\nu}\right)^2 \mathcal{C} + \mathcal{O}\left(\frac{\nu_0}{E_\nu}\right)^3\right], \tag{7.1}$$

where the coefficients are $\mathcal{A} = \mathcal{F}_2, \mathcal{B} = (\mathcal{F}_2 \pm \mathcal{F}_3)/2, \mathcal{C} = (\mathcal{F}_2 \mp \mathcal{F}_3)/6$, and $\mathcal{F}_i = \int_0^1 \int_0^{\nu_0} F_i(x) dx d\nu$ is the integral of structure function $F_i(x)$. The dynamics of neutrino-nucleon scattering implies that the number of events in a given energy bin with hadronic energy $E_{\rm had} < \nu_0$ is proportional to the (anti)neutrino flux in that energy bin up to corrections $\mathcal{O}(\nu_0/E_\nu)$ and $\mathcal{O}(\nu_0/E_\nu)^2$. The number $\mathcal{N}(\nu < \nu_0)$ is therefore proportional to the flux up to correction factors of the order $\mathcal{O}(\nu_0/E_\nu)$ or smaller, which are not significant for small values of ν_0 at energies $\geq \nu_0$. The coefficients $\mathcal{A}$, $\mathcal{B}$ and $\mathcal{C}$ are determined for each energy bin and neutrino flavor within the ND data.

LBNE's primary interest is the relative flux determination, i.e., the neutrino flux in one energy bin relative to that in another; variations in the coefficients do not affect the relative flux. The prescription for the relative flux determination is simple: count the number of neutrino CC events below a certain small value of hadronic energy (ν_0). The observed number of events, up to the correction of the order $\mathcal{O}(\nu_0/E_\nu)$ due to the finite ν_0 in each total visible energy bin, is proportional to the relative flux. The smaller the factor ν_0/E_ν is, the smaller is the correction. Furthermore, the energy of events passing the low-ν_0 cut is dominated by the corresponding lepton energy.

It is apparent from the above discussion that this method of relative flux determination is not very sensitive to nucleon structure, QCD corrections or types of neutrino interactions such as scaling or nonscaling. With the excellent granularity and resolution foreseen in the low-density magnetized tracker, it will be possible to use a value of ν_0 ~0.5 GeV or lower, thus allowing flux predictions down to E_ν ~0.5 GeV. A preliminary analysis with the high-resolution tracker achieved a precision $\leq 2\%$ on the relative ν_μ flux with the low-ν_0 method in the energy region $1 \leq E_\nu \leq 30$ GeV in the fit with $\nu_0 < 0.5$ GeV. Similar uncertainties are expected for the $\overline{\nu}_\mu$ component (the dominant one) in the antineutrino beam mode (negative focusing).

7.1.2 Determination of the Flavor Content of the Beam: $\nu_\mu, \overline{\nu}_\mu, \nu_e, \overline{\nu}_e$

The empirical parameterization of the pion and kaon neutrino parents produced from the proton target, determined from the low-ν_0 flux at the ND, allows prediction of the ν_μ and $\overline{\nu}_\mu$ flux at the far detector location. This parameterization provides a measure of the $\pi^+/K^+/\mu^+(\pi^-/K^-/\mu^-)$ distributions of neutrino parents of the beam observed in the ND. Additionally, with the capability to identify $\overline{\nu}_e$ CC interactions, it is possible to directly extract the elusive K^0_L content of the beam. Therefore, an accurate measurement of the $\nu_\mu, \overline{\nu}_\mu$ and $\overline{\nu}_e$ CC interactions provides a prediction of the ν_e content of the beam, which is an irreducible background for the ν_e appearance search in the far detector:

$$\nu_e \equiv \mu^+(\pi^+ \to \nu_\mu) \oplus K^+(K^+ \to \nu_\mu) \oplus K_L^0 \tag{7.2}$$
$$\overline{\nu}_e \equiv \mu^-(\pi^- \to \overline{\nu}_\mu) \oplus K^-(K^- \to \overline{\nu}_\mu) \oplus K_L^0 \tag{7.3}$$

The μ component is well constrained from $\nu_\mu(\overline{\nu}_\mu)$ CC data at low energy, while the $K^\pm$ component is only partially constrained by the $\nu_\mu(\overline{\nu}_\mu)$ CC data at high energy and requires external hadro-production measurements of $K^\pm/\pi^\pm$ ratios at low energy from hadro-production experiments such as MIPP [6] and NA61 [7]. Finally, the K_L^0 component can be constrained by the $\overline{\nu}_e$ CC data and by external dedicated measurements at hadron-production experiments. In the energy range $1(5) \leq E_\nu \leq 5(15)$ GeV, the approximate relative contributions to the ν_e spectrum are 85% (55%) from μ^+, 10% (30%) from K^+ and 3% (15%) from K_L^0.

Based on the NOMAD experience, a precision of $\leq 0.1\%$ on the flux ratio ν_e/ν_μ is expected at high energies. Taking into account the projected precision of the ν_μ flux discussed in Section 7.1.1, this translates into an absolute prediction for the ν_e flux at the level of 2%.

Finally, the fine-grained ND can directly identify ν_e CC interactions from the LBNE beam. The relevance of this measurement is twofold:

1. It provides an independent validation for the flux predictions obtained from the low-ν_0 method.
2. It can further constrain the uncertainty on the knowledge of the absolute ν_e flux.

7.1.3 Constraining the Unoscillated ν Spectral Shape with the QE Interaction

In any long-baseline neutrino oscillation program, including LBNE, the quasi-elastic (QE) interactions are special. First, the QE cross section is substantial at lower energies [8]. Second, because of the simple topology (a μ^- and a proton), the visible interaction energy provides, to first order, a close approximation to the neutrino energy (E_ν). In the context of a fine-grained tracker, a precise measurement of QE will impose direct constraints on nuclear effects related to both the primary and final-state interaction (FSI) dynamics (Section 7.6), which can affect the overall neutrino energy scale and, thus, the entire oscillation program. To this end, the key to reconstructing a high-quality sample of ν_μ QE interactions is the two-track topology where both final-state particles are visible: μ^- and p. A high-resolution ND can efficiently identify the recoil proton and measure its momentum vector as well as dE/dx. Preliminary studies indicate that in a fine-grained tracking detector the efficiency (purity) for the proton reconstruction in QE events is 52% (82%). A comparison between the neutrino energy reconstructed from the muon momentum through the QE kinematics (assuming a free target nucleon) with the visible neutrino energy measured as the sum of μ and p energies is sensitive to both nuclear effects and FSI. Furthermore, comparing the two-track sample

(μ and p) with the single-track sample (in which only μ is reconstructed) empirically constrains the rate of FSI.

7.1.4 Low-Energy Absolute Flux: Neutrino-Electron NC Scattering

Neutrino neutral current (NC) interaction with the atomic electron in the target, $\nu_\mu e^- \to \nu_\mu e^-$, provides an elegant measure of the absolute flux. The total cross section for NC elastic scattering off electrons is given by [9]:

$$\sigma(\nu_l e \to \nu_l e) = \frac{G_\mu^2 m_e E_\nu}{2\pi}\left[1 - 4\sin^2\theta_W + \frac{16}{3}\sin^4\theta_W\right], \tag{7.4}$$

$$\sigma(\overline{\nu}_l e \to \overline{\nu}_l e) = \frac{G_\mu^2 m_e E_\nu}{2\pi}\left[\frac{1}{3} - \frac{4}{3}\sin^2\theta_W + \frac{16}{3}\sin^4\theta_W\right], \tag{7.5}$$

where θ_W is the weak mixing angle (WMA). For the currently known value of $\sin^2\theta_W \simeq 0.23$, the above cross sections are very small: $\sim 10^{-42}(E_\nu/\mathrm{GeV})$ cm^2. The NC elastic scattering off electrons can be used to determine the absolute flux normalization since the cross section only depends on the knowledge of $\sin^2\theta_W$. Within the Standard Model, the value of $\sin^2\theta_W$ at the average momentum transfer expected at LBNE, $Q \sim 0.07$ GeV, can be extrapolated down from the LEP/SLC* measurements with a precision of $\leq 1\%$. The $\nu_\mu e^- \to \nu_\mu e^-$ will produce a single e^- collinear with the ν-beam (≤ 40 mrad). The background, dominated by the asymmetric conversion of a photon in an ordinary ν-nucleon NC event, will produce e^- and e^+ in equal measure with much broader angular distribution. A preliminary analysis of the expected elastic scattering signal in the high-resolution tracking ND shows that the scattering signal can be selected with an efficiency of about 60% with a small background contaminant. The measurement will be dominated by the statistical error. The determination of the absolute flux of the LBNE neutrinos is estimated to reach a precision of $\simeq 2.5\%$ for $E_\nu \leq 10$ GeV. The measurement of NC elastic scattering off electrons can only provide the integral of all neutrino flavors.

7.1.5 High-Energy Absolute Flux: Neutrino-Electron CC Scattering

The ν_μ-e^- CC interaction, $\nu_\mu + e^- \to \mu^- + \nu_e$ (*inverse muon decay* or *IMD*), offers an elegant way to determine the absolute flux. Given the energy threshold needed for this process, IMD requires $E_\nu \geq 10.8$ GeV. The high-resolution ND in the LBNE neutrino beam will observe $\geq$ 2,000 IMD events in three years. The reconstruction efficiency of the single, energetic forward μ^- will be $\geq$ 98%; the angular resolution of the IMD μ is ≤ 1 mrad. The background, primarily from the ν_μ-QE interactions, can be precisely constrained using control samples. In particular, the systematic limitations of the CCFR ([10,11]) and the CHARM-II [12] IMD measurements can be substantially

*LEP was the Large Electron-Positron Collider at CERN that operated from 1989 to 2000 and provided a detailed study of the electroweak interaction.

alleviated in LBNE with the proposed ND design. A preliminary analysis indicates that the absolute flux can be determined with an accuracy of $\approx 3\%$ for $E_\nu \geq 11$ GeV (average $E_\nu \approx$25 GeV).

7.1.6 Low-Energy Absolute Flux: QE in Water and Heavy-Water Targets

Another independent method to extract the absolute flux is through the QE-CC scattering ($\nu_\mu n(p) \to \mu^- p(n)$) on deuterium at low Q^2. Neglecting terms in $(m_\mu/M_n)^2$ at $Q^2 = 0$, the QE cross section is independent of neutrino energy for $(2E_\nu M_n)^{1/2} > m_\mu$:

$$\frac{d\sigma}{dQ^2} \mid Q^2 = 0 \mid = \frac{G_\mu^2 \cos^2\theta_c}{2\pi} \left[F_1^2(0) + G_A^2(0)\right] = 2.08 \times 10^{-38}\ \mathrm{cm}^2\mathrm{GeV}^{-2}, \tag{7.6}$$

which is determined by neutron β decay and has a theoretical uncertainty $< 1\%$. The flux can be extracted experimentally by measuring low Q^2 QE interactions (≤ 0.05 GeV) and extrapolating the result to the limit of $Q^2 = 0$. The measurement requires a deuterium (or hydrogen for antineutrino) target to minimize the smearing due to Fermi motion and other nuclear effects. This requirement can only be achieved by using both H_2O and D_2O targets embedded in the fine-grained tracker and extracting the events produced in deuterium by statistical subtraction of the larger oxygen component. The experimental resolution on the muon and proton momentum and angle is crucial. Dominant uncertainties of the method are related to the extrapolation to $Q^2 = 0$, to the theoretical cross section on deuterium, to the experimental resolution and to the statistical subtraction. Sensitivity studies and the experimental requirements are under study.

7.1.7 Neutral Pions, Photons and $\pi^\pm$ in NC and CC Events

The principal background to the ν_e and $\overline{\nu}_e$ appearance comes from the NC events where a photon from the π^0 decay produces a signature similar to that produced by ν_e-induced electron; the second source of background is due to π^0's from ν_μ CC where the μ^- evades identification — typically at high y_{Bj}. Since the energy spectra of NC and CC interactions are different, it is critical for the ND to measure π^0's in NC and CC interactions in the full kinematic phase space.

The proposed ND is designed to measure π^0's with high accuracy in three topologies:

1. Both photons convert in the tracker ($\simeq$25%).

2. One photon converts in the tracker and the other in the calorimeter ($\simeq$50%).

3. Both photons convert in the calorimeter; the first two topologies afford the best resolution because the tracker provides precise γ-direction measurement.

The π^0 reconstruction efficiency in the proposed fine-grained tracker is expected to be $\geq$75% if photons that reach the ECAL are included. By contrasting the π^0 mass in the tracker versus in the calorimeter, the relative efficiencies of photon reconstruction will be well constrained.

Finally, the $\pi^{\pm}$ track momentum and dE/dx information will be measured by the tracker. An in situ determination of the charged pions in the $\nu_\mu/\overline{\nu}_\mu$ CC events — with μID and without μID — and in the ν NC events is crucial to constrain the systematic error associated with the $\nu_\mu(\overline{\nu}_\mu)$ disappearance, especially at low E_ν.

7.1.8 Signal and Background Predictions for the Far Detector

In order to achieve reliable predictions for signal and backgrounds in the far detector, near detector measurements — including (anti)neutrino fluxes, nuclear cross sections and detector smearing — must be unfolded and extrapolated to the far detector location. The geometry of the beam and detectors (point source versus extended source) as well as the expected neutrino oscillations imply differences in the (anti)neutrino fluxes in the near and far detectors. These differences, in turn, will result in increased sensitivity of the long-baseline analysis to cross-section uncertainties, in particular between neutrinos and antineutrinos and for exclusive background topologies. Furthermore, the much higher event rates at the near site and the smaller detector size (i.e., reduced containment) make it virtually impossible to achieve identical measurement conditions in both the near and far detectors. However, as discussed in Sections 7.1.1 to 7.1.7, the energy, angular and space resolution of the low-density ND are key factors in reducing the systematic uncertainties achievable on the event predictions for the far detector; the ND can offer a precise *in situ* measurement of the absolute flux of all flavor components of the beam, $\nu_\mu, \nu_e, \bar{\nu}_\mu, \bar{\nu}_e$, resulting in constraints on the parent $\pi^{\pm}/K^{\pm}/\mu^{\pm}$ distributions. In addition, measurements of momenta and energies of final-state particles produced in (anti)neutrino interactions will allow a detailed study of exclusive topologies affecting the signal and background rates in the far detector. All of these measurements will be used to cross-check and fine-tune the simulation programs needed for the actual extrapolation from the near to the far detector.

It is important to note that several of these techniques have already been used and *proven to work* in neutrino experiments such as MINOS [13] and NOMAD [14,15,16]. The higher segmentation and resolution in the LBNE ND with respect to past experiments will increase the available information about the (anti)neutrino event topologies, allowing further reduction of systematic uncertainties both in the ND measurements and in the Monte Carlo extrapolation.

For a more detailed discussion of the impact of ND measurements on the long-baseline oscillation analysis see Section 4.3.2.

7.2 Electroweak Precision Measurements

Neutrinos and antineutrinos are the most effective probes for investigating electroweak physics. Interest in a precise determination of the weak mixing angle ($\sin^2\theta_W$) at LBNE energies via neutrino scattering is twofold: (1) it provides a direct measurement of neutrino couplings to the Z boson and (2) it probes a different scale of momentum transfer than LEP did by virtue of not being at the Z boson mass peak.

The weak mixing angle can be extracted experimentally from three main NC physics processes:

1. deep inelastic scattering off quarks inside nucleons: $\nu N \to \nu X$
2. elastic scattering off electrons: $\nu e^- \to \nu e^-$
3. elastic scattering off protons: $\nu p \to \nu p$

Figure 7.1 shows the Feynman diagrams corresponding to the three processes.

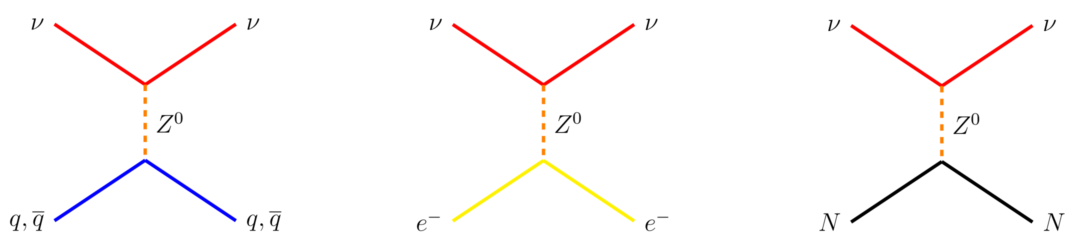

Figure 7.1: Feynman diagrams for the three main neutral current processes that can be used to extract $\sin^2\theta_W$ with the LBNE near detector. From left, deep inelastic scattering off quarks, elastic scattering off electrons and elastic scattering off nucleons.

7.2.1 Deep Inelastic Scattering

The most precise measurement of $\sin^2\theta_W$ in neutrino deep inelastic scattering (DIS) comes from the NuTeV experiment, which reported a value that is 3σ from the Standard Model [17]. The LBNE ND can perform a similar analysis in the DIS channel by measuring the ratio of NC and CC interactions induced by neutrinos:

$$\mathcal{R}^\nu \equiv \frac{\sigma^\nu_{\rm NC}}{\sigma^\nu_{\rm CC}} \simeq \rho^2 \left(\frac{1}{2} - \sin^2\theta_W + \frac{5}{9}(1+r)\sin^4\theta_W\right). \tag{7.7}$$

Here ρ is the relative coupling strength of the neutral-to-charged current interactions ($\rho = 1$ at tree-level in the Standard Model) and r is the ratio of antineutrino to neutrino cross section ($r \sim 0.5$).

The absolute sensitivity of $\mathcal{R}^\nu$ to $\sin^2\theta_W$ is 0.7, which implies that a measurement of $\mathcal{R}^\nu$ to 1% precision would in turn provide a 1.4% precision on $\sin^2\theta_W$. This technique was used by the CDHS [18], CHARM [19] and CCFR [20] experiments. In contrast to the NuTeV experiment, the antineutrino interactions cannot be used for this analysis at LBNE due to the large number of ν_μ DIS interactions in the $\overline{\nu}_\mu$ beam compared to the $\overline{\nu}_\mu$ DIS interactions.

The measurement of $\sin^2\theta_W$ from DIS interactions can only be performed with a low-density magnetized tracker since an accurate reconstruction of the NC event kinematics and of the ν CC interactions are crucial for keeping the systematic uncertainties on the event selection under control. The analysis selects events in the ND after imposing a cut on the visible hadronic energy of $E_{\text{had}} > 5\,\text{GeV}$ (the CHARM analysis had $E_{\text{had}} > 4\,\text{GeV}$). With an exposure of 5×10^{21} POT in the 120-GeV beam using the CDR reference design, about 7.7×10^6 CC events and 2.4×10^6 NC events are expected, giving a statistical precision of 0.074% on $\mathcal{R}^\nu$ and 0.1% on $\sin^2\theta_W$ (Table 7.2).

Table 7.2: Comparison of uncertainties on the $\mathcal{R}^\nu$ measurement between NuTeV and LBNE with a 5 t fiducial mass after an exposure of 5×10^{21} POT (5 year) with the CDR reference 120-GeV beam. The corresponding relative uncertainties on $\sin^2\theta_W$ must be multiplied by a factor of 1.4, giving for LBNE a projected overall precision of 0.35%.

Source of uncertainty	$\delta R^\nu/R^\nu$		Comments
	NuTeV	LBNE	
Data statistics	0.00176	0.00074	
Monte Carlo statistics	0.00015		
Total Statistics	*0.00176*	*0.00074*	
$\nu_e,\overline{\nu}_e$ **flux** ($\sim$ **1.7%**)	0.00064	0.00010	e^-/e^+ identification
Energy measurement	0.00038	0.00040	
Shower length model	0.00054	n.a.	
Counter efficiency, noise	0.00036	n.a.	
Interaction vertex	0.00056	n.a.	
$\overline{\nu}_\mu$ **flux**	n.a.	0.00070	Large $\bar{\nu}$ contamination
Kinematic selection	n.a.	0.00060	Kinematic identification of NC
Experimental systematics	*0.00112*	*0.00102*	
d,s→c, s-sea	0.00227	0.00140	Based on existing knowledge
Charm sea	0.00013	n.a.	
$r = \sigma^{\overline{\nu}}/\sigma^\nu$	0.00018	n.a.	
Radiative corrections	0.00013	0.00013	
Non-isoscalar target	0.00010	N.A.	
Higher twists	0.00031	0.00070	Lower Q^2 values
R_L (F_2, F_T, xF_3)	0.00115	0.00140	Lower Q^2 values
Nuclear correction		0.00020	
Model systematics	*0.00258*	*0.00212*	
Total	**0.00332**	**0.00247**	

The use of a low-density magnetized tracker can substantially reduce systematic uncertainties compared to a massive calorimeter. Table 7.2 shows a comparison of the different uncertainties on the measured $\mathcal{R}^\nu$ between NuTeV and LBNE. While NuTeV measured both $\mathcal{R}^\nu$ and $\mathcal{R}^{\overline{\nu}}$, the largest experimental uncertainty in the measurement of $\mathcal{R}^\nu$ is related to the subtraction of the ν_e CC contamination from the NC sample. Since the low-density tracker at LBNE can efficiently reconstruct the electron tracks, the ν_e CC interactions can be identified on an event-by-event basis, reducing the corresponding uncertainty to a negligible level. Similarly, uncertainties related to the location of the interaction vertex, noise, counter efficiency and so on are removed by the higher resolution and by changing the analysis selection. The experimental selection at LBNE will be dominated by two uncertainties: the knowledge of the $\overline{\nu}_\mu$ flux and the kinematic selection of NC interactions. The former is relevant due to the larger NC/CC ratio for antineutrinos. The total experimental systematic uncertainty on $\sin^2\theta_W$ is expected to be about 0.14%.

The measurement of $\mathcal{R}^\nu$ will be dominated by theoretical systematic uncertainties on the structure functions of the target nucleons. The estimate of these uncertainties for LBNE is based upon the extensive work performed for the NOMAD analysis and includes a Next-to-Next-Leading-Order (NNLO) QCD calculation of structure functions (NLO for charm production) [21,22,23], parton distribution functions (PDFs) extracted from dedicated low-Q global fits, high-twist contributions [21], electroweak corrections [24] and nuclear corrections [25,26,27]. The charm quark production in CC, which has been the dominant source of uncertainty in all past determinations of $\sin^2\theta_W$ from νN DIS, is reduced to about 4% of the total ν_μ CC DIS for $E_{\text{had}} > 5$ GeV with the low-energy beam spectrum at LBNE. This number translates into a systematic uncertainty of 0.14% on $\mathcal{R}^\nu$ (Table 7.2), assuming the current knowledge of the charm production cross section. It is worth noting that the recent measurement of charm dimuon production by the NOMAD experiment allowed a reduction of the uncertainty on the strange sea distribution to $\sim 3\%$ and on the charm quark mass m_c to ~ 75 MeV [16]. The lower neutrino energies available at LBNE reduce the accessible Q^2 values with respect to NuTeV, increasing in turn the effect of non-perturbative contributions (high twists) and R_L. The corresponding uncertainties are reduced by the recent studies of low-Q structure functions and by improved modeling with respect to the NuTeV analysis (NNLO vs. LO). The total model systematic uncertainty on $\sin^2\theta_W$ is expected to be about 0.21% with the reference beam configuration. The corresponding total uncertainty on the value of $\sin^2\theta_W$ extracted from νN DIS is 0.35%.

Most of the model uncertainties will be constrained by dedicated in situ measurements using the large CC samples and employing improvements in theory that will have evolved over the course of the experiment. The low-density tracker will collect about 350,000 neutrino-induced inclusive charm events in a five-year run with the 120-GeV 1.2-MW beam. The precise reconstruction of charged tracks will allow measurement of exclusive decay modes of charmed hadrons (e.g., D^{*+}) and measurement of charm fragmentation and production parameters. The average semileptonic branching ratio B_μ is of order 5% with the low-energy LBNE beam, and the low-density ND will be able to reconstruct both the $\mu\mu$ and μe decay channels. Currently, the most precise sample of 15,400 dimuon events has been collected by the NOMAD experiment. Finally, precision measurements of CC structure functions in the LBNE ND would further reduce the uncertainties on PDFs and on high-twist contributions.

The precision that can be achieved from νN DIS interactions is limited by both the event rates and the energy spectrum of the standard beam configuration. The high-statistics beam exposure with the low-energy default beam-running configuration (described in Chapter 3) combined with a dedicated run with the high-energy beam option would increase the statistics by more than a factor of ten. This major step forward would not only reduce the statistical uncertainty to a negligible level, but would provide large control samples and precision auxiliary measurements to reduce the systematic uncertainties on structure functions. The two dominant systematic uncertainties, charm production in CC interactions and low Q^2 structure functions, are essentially defined by the available data at present. Overall, the use of a high-energy beam with upgraded intensity can potentially improve the precision achievable on $\sin^2\theta_W$ from νN DIS to better than 0.2%.

7.2.2 Elastic Scattering

A second independent measurement of $\sin^2\theta_W$ can be obtained from NC $\nu_\mu e$ elastic scattering. This channel has lower systematic uncertainties since it does not depend on knowledge of the structure of nuclei, but it has limited statistics due to its very low cross section. The value of $\sin^2\theta_W$ can be extracted from the ratio of interactions [9] as follows:

$$\mathcal{R}_{\nu e}(Q^2) \equiv \frac{\sigma(\overline{\nu}_\mu e \to \overline{\nu}_\mu e)}{\sigma(\nu_\mu e \to \nu_\mu e)}(Q^2) \simeq \frac{1 - 4\sin^2\theta_W + 16\sin^4\theta_W}{3 - 12\sin^2\theta_W + 16\sin^4\theta_W}, \tag{7.8}$$

in which systematic uncertainties related to the selection and the electron identification cancel out. The absolute sensitivity of this ratio to $\sin^2\theta_W$ is 1.79, which implies that a measurement of $\mathcal{R}_{\nu e}$ to 1% precision would provide a measurement of $\sin^2\theta_W$ to 0.65% precision.

The best measurement of NC elastic scattering off electrons was performed by CHARM II, which observed 2677$\pm$82 ν and 2752$\pm$88 $\overline{\nu}$ events [28]. The CHARM II analysis was characterized by a sizable uncertainty related to the extrapolation of the background into the signal region.

The event selection for NC elastic scattering is described in Section 7.1.4. Since the NC elastic scattering off electrons is also used for the absolute flux normalization, the WMA analysis can be performed only with the low-density, magnetized tracker in conjunction with a large liquid argon detector. In the case of the flux normalization measurement, the total reconstructed statistics is limited to about 4,500 (2,800) $\nu(\overline{\nu})$ events. These numbers do not allow a competitive determination of $\sin^2\theta_W$ by using the magnetized tracker alone. However, a 100-t liquid argon detector in the ND would be expected to collect about 90,000 (60,000) reconstructed $\nu(\overline{\nu})$ events with the standard beam, and an additional factor of two with an upgraded 2.3-MW beam.

A combined analysis of both detectors can achieve the optimal sensitivity: the fine-grained tracker is used to reduce systematic uncertainties (measurement of backgrounds and calibration), while the liquid argon detector provides the statistics required for a competitive measurement. Overall, the use of the complementary liquid argon detector can provide a statistical accuracy on $\sin^2\theta_W$ of about 0.3%. However, the extraction of the WMA is dominated by the systematic uncertainty on the $\overline{\nu}_\mu/\nu_\mu$ flux ratio in Equation (7.8). This uncertainty has been evaluated with the low-ν_0 method for the flux extraction and a systematic uncertainty of about 1% was obtained on the ratio of the $\overline{\nu}_\mu/\nu_\mu$ flux integrals. An improved precision on this quantity could be achieved from a measurement of the ratios π^-/π^+ and ρ^-/ρ^+ from coherent production in the fine-grained tracker. Due to the excellent angular and momentum resolution and to large cancellations of systematic uncertainties, preliminary studies indicate that an overall precision of about 0.3% can be achieved on the $\overline{\nu}_\mu/\nu_\mu$ flux ratio using coherent production.

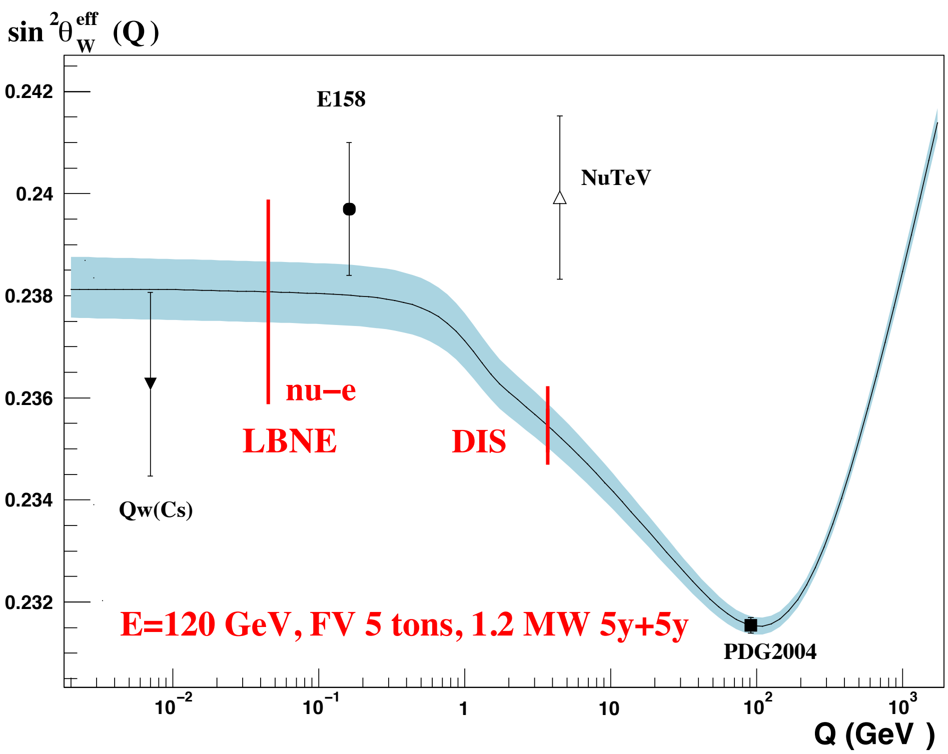

Figure 7.2: Expected sensitivity to the measurement of $\sin^2\theta_W$ from the LBNE ND with the reference 1.2-MW beam and an exposure of 5×10^{21} POT with a neutrino beam (five years) and 5×10^{21} POT with an antineutrino beam (five years). The curve shows the Standard Model prediction as a function of the momentum scale [29]. Previous measurements from Atomic Parity Violation [30,31], Moeller scattering (E158 [32]), ν DIS (NuTeV [17]) and the combined Z pole measurements (LEP/SLC) [31] are also shown for comparison. The use of a high-energy beam tune can reduce the LBNE uncertainties by almost a factor of two.

Together, the DIS and the NC elastic scattering channels involve substantially different scales of momentum transfer, providing a tool to test the running of $\sin^2\theta_W$ in a single experiment. To this end, the study of NC elastic scattering off protons can provide additional information since it occurs at a momentum scale that is intermediate between the two other processes. Figure 7.2 summarizes the target sensitivity from the LBNE ND, compared with existing measurements as a function of the momentum scale.

In the near future, another precision measurement of $\sin^2\theta_W$ is expected from the $Q_{\rm weak}$ experiment [33] at Jefferson Laboratory. From the measurement of parity-violating asymmetry in elastic electron-proton scattering, the $Q_{\rm weak}$ experiment should achieve a precision of 0.3% on $\sin^2\theta_W$ at $Q^2 = 0.026$ GeV^2. It should be noted that the $Q_{\rm weak}$ measurement is complementary to those from neutrino scattering given the different scale of momentum transfer and the fact that neutrino measurements are the only direct probe of the Z coupling to neutrinos. With the 12-GeV upgrade of Jefferson Laboratory, the Q_{weak} experiment [34] could potentially reach precisions on the order of 0.2-0.1 %.

7.3 Observation of the Nucleon's Strangeness Content

The strange-quark content of the proton and its contribution to the proton spin remain enigmatic [35]. The question is whether the strange quarks contribute substantially to the vector and axial-vector currents of the nucleon. A large observed value of the strange-quark contribution to the nucleon spin (axial current), Δs, would enhance our understanding of the proton structure.

The spin structure of the nucleon also affects the couplings of axions and supersymmetric particles to dark matter.

7.3.1 Strange Form Factors of Nucleons

The strange quark *vector* elastic form factors† of the nucleon have been measured to high precision in parity-violating electron scattering (PVES) at Jefferson Lab, Mainz and elsewhere. A recent global analysis [36] of PVES data finds a strange magnetic moment $\mu_s = 0.37 \pm 0.79$ (in units of the nucleon magneton), so that the strange quark contribution to proton magnetic moment is less than 10%. For the strange electric charge radius parameter, ρ_s, one finds a very small value, $\rho_s = -0.03 \pm 0.63$ GeV^{-2}, consistent with zero. Both results are consistent with theoretical expectations based on lattice QCD and phenomenology [37].

In contrast, the strange *axial vector* form factors are poorly determined. A global study of PVES

†Nucleon form factors describe the scattering amplitudes off different partons in a nucleon. They are usually given as a function of Q^2 the momentum transfer to the nucleon from the scattering lepton (since the structure of the nucleon looks different depending on the energy of the probe).

data [36] finds $\widetilde{G}_A^N(Q^2) = \widetilde{g}_A^N\,(1 + Q^2/M_A^2)^2$, where $M_A = 1.026$ GeV is the axial dipole mass, with the effective proton and neutron axial charges $\widetilde{g}_A^p = -0.80 \pm 1.68$ and $\widetilde{g}_A^n = 1.65 \pm 2.62$.

The strange quark axial form factor at $Q^2 = 0$ is related to the *spin* carried by strange quarks, Δs. Currently the world data on the spin-dependent g_1 structure function constrain Δs to be ≈ -0.055 at a scale $Q^2 = 1$ GeV^2, with a significant fraction coming from the region $x < 0.001$.

An independent extraction of Δs, which does not rely on the difficult measurements of the g_1 structure function at very small values of the Bjorken variable x, can be obtained from (anti)neutrino NC elastic scattering off protons (Figure 7.3). Indeed, this process provides the most direct measurement of Δs. The differential cross section for NC-elastic and CC-QE scattering of (anti)neutrinos from protons can be written as:

$$\frac{d\sigma}{dQ^2} = \frac{G_\mu^2}{2\pi}\frac{Q^2}{E_\nu^2}\left(A \pm BW + CW^2\right); \quad W = 4E_\nu/M_p - Q^2/M_p^2, \tag{7.9}$$

where the positive (negative) sign is for neutrino (antineutrino) scattering and the coefficients A, B, and C contain the vector and axial form factors as follows:

$$\begin{aligned} A &= \frac{1}{4}\left[G_1^2\,(1+\tau) - \left(F_1^2 - \tau F_2^2\right)(1-\tau) + 4\tau F_1 F_2\right] \\ B &= -\frac{1}{4}G_1\,(F_1 + F_2) \\ C &= \frac{1}{16}\frac{M_p^2}{Q^2}\left(G_1^2 + F_1^2 + \tau F_2^2\right) \end{aligned}$$

The axial-vector form factor, G_1, for NC scattering can be written as the sum of the known axial form factor G_A plus a strange form factor G_A^s:

$$G_1 = \left[-\frac{G_A}{2} + \frac{G_A^s}{2}\right], \tag{7.10}$$

while the NC vector form factors can be written as:

$$F_{1,2} = \left[\left(\frac{1}{2} - \sin^2\theta_W\right)\left(F_{1,2}^p - F_{1,2}^n\right) - \sin^2\theta_W\left(F_{1,2}^p + F_{1,2}^n\right) - \frac{1}{2}F_{1,2}^s\right], \tag{7.11}$$

where $F_1^{p(n)}$ is the Dirac form factor of the proton (neutron), $F_2^{p(n)}$ is the corresponding Pauli form factor, and $F_{1,2}^s$ are the strange-vector form factors. These latter form factors are expected to be small from the PVES measurements summarized above. In the limit $Q^2 \to 0$, the differential cross section is proportional to the square of the axial-vector form factor $d\sigma/dQ^2 \propto G_1^2$ and $G_A^s \to \Delta s$. The value of Δs can therefore be extracted experimentally by extrapolating the NC differential cross section to $Q^2 = 0$.

7.3.2 Extraction of the Strange Form Factors

Previous neutrino scattering experiments have been limited by the statistics and by the systematic uncertainties on background subtraction. One of the earliest measurements available comes from the analysis of 951 NC νp and 776 NC $\overline{\nu} p$ collected by the experiment BNL E734 [38,39,40]. There are also more recent results with high statistics from MiniBooNE where a measurement of Δs was carried out using neutrino NC elastic scattering with 94,531 νN events [41]. The MiniBooNE measurement was limited by the inability to distinguish the proton and neutron from νN scattering. The LBNE neutrino beam will be sufficiently intense that a measurement of NC elastic scattering on protons in the fine-grained ND can provide a definitive statement on the contribution of the strange sea to either the axial or vector form factor.

Systematic uncertainties can be reduced by measuring the NC/CC ratios for both neutrinos and antineutrinos as a function of Q^2:

$$\mathcal{R}_{\nu p}(Q^2) \equiv \frac{\sigma(\nu_\mu p \to \nu_\mu p)}{\sigma(\nu_\mu n \to \mu^- p)}(Q^2); \qquad \mathcal{R}_{\overline{\nu} p}(Q^2) \equiv \frac{\sigma(\overline{\nu}_\mu p \to \overline{\nu}_\mu p)}{\sigma(\overline{\nu}_\mu p \to \mu^+ n)}(Q^2), \tag{7.12}$$

Figure 7.3 shows the absolute sensitivity of both ratios to Δs for different values of Q^2. The sensitivity for $Q^2 \sim 0.25$ GeV^2 is about 1.2 for neutrinos and 1.9 for antineutrinos, which implies that a measurement of $\mathcal{R}_{\nu p}$ and $\mathcal{R}_{\overline{\nu} p}$ of 1% precision would enable the extraction of Δs with an uncertainty of 0.8% and 0.5%, respectively.

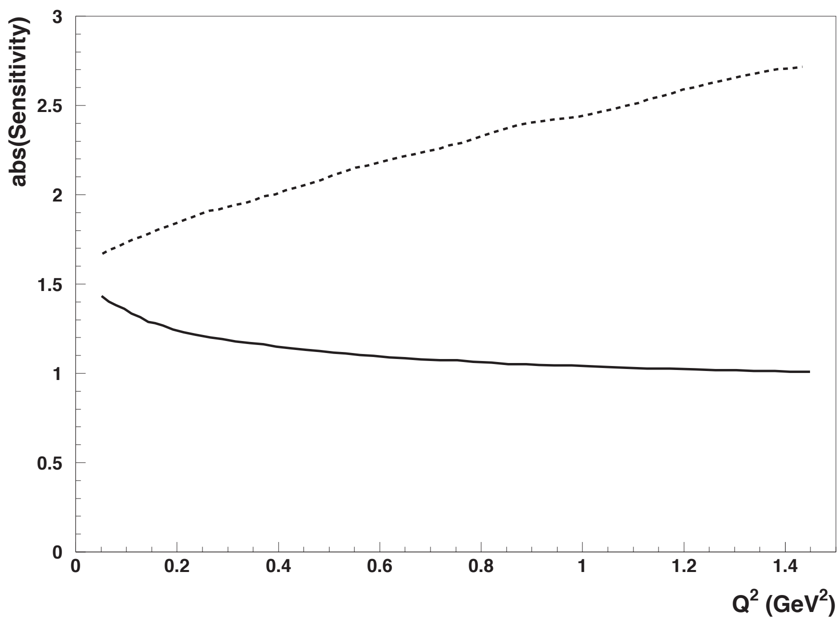

Figure 7.3: Sensitivity (magnitude) of the ratios $\mathcal{R}_{\nu p}$ (solid) and $\mathcal{R}_{\overline{\nu} p}$ (dashed) to a variation of the strange contribution to the spin of the nucleon, Δs, as a function of Q^2. Values greater than one imply that the relative uncertainty on Δs is smaller than that of the corresponding ratio (see text).

The design of the tracker includes several different nuclear targets. Therefore, most of the neutrino scattering is from nucleons embedded in a nucleus, requiring nuclear effects to be taken into account. Fortunately, in the ratio of NC/CC, the nuclear corrections are expected to largely cancel out. The Δs analysis requires a good proton reconstruction efficiency as well as high resolution on both the proton angle and energy. To this end, the low-density tracker can increase the range of the protons inside the ND, allowing the reconstruction of proton tracks down to $Q^2 \sim 0.07\,\text{GeV}^2$. This capability will reduce the uncertainties in the extrapolation of the form factors to the limit $Q^2 \to 0$.

Table 7.3 summarizes the expected proton range for the low-density ($\rho \sim 0.1\,\text{g}\,\text{cm}^{-3}$) straw-tube tracker (STT) in the ND tracking detector design described in Section 3.5. About $2.0(1.2) \times 10^6$ $\nu p(\overline{\nu} p)$ events are expected after the selection cuts in the low-density tracker, yielding a statistical precision on the order of 0.1%.

Table 7.3: Expected proton range for the low-density (ρ ~$0.1\,\text{g}\,\text{cm}^{-3}$) tracker. The first column gives the proton kinetic energy and the last column the proton momentum. The Q^2 value producing T_p is calculated assuming the struck nucleon is initially at rest.

T_p MeV	Q^2 GeV^2/c^2	Range STT cm	P_p GeV/c
20	0.038	4.2	0.195
40	0.075	14.5	0.277
60	0.113	30.3	0.341
80	0.150	50.8	0.395
100	0.188	75.7	0.445

The determination of Δs in the STT utilizes analysis techniques performed by the FINeSSE Collaboration [42] and used by the SciBooNE experiment. In particular, based on the latter, LBNE expects a purity of about 50%, with background contributions of 20% from neutrons produced outside of the detector, 10% νn events and 10% NC pion backgrounds. The dominant systematic uncertainty will be related to the background subtraction. The low-energy beam spectrum at LBNE provides the best sensitivity for this measurement since the external background from neutron-induced proton recoils will be reduced by the strongly suppressed high-energy tail. The low-density magnetized tracker is expected to increase the purity by reducing the neutron background and the NC pion background. The outside neutron background, it should be noted, can be determined using the $n \to p + \pi^-$ process in the STT. The sensitivity analysis is still in progress, however LBNE is confident of achieving a precision on Δs of about 0.02–0.03.

7.4 Nucleon Structure and QCD Studies

Precision measurements of (anti)neutrino differential cross sections in the LBNE near detector will provide additional constraints on several key nucleon structure functions that are complementary to results from electron scattering experiments.

In addition, these measurements would directly improve LBNE's oscillation measurements by providing accurate simulation of neutrino interactions in the far detector and offer an estimate of all background processes that are dependent upon the angular distribution of the outgoing particles in the far detector. Furthermore, certain QCD analyses — i.e., global fits used for extraction of parton distribution functions (PDFs) via the differential cross sections measured in ND data — would constrain the systematic error in precision electroweak measurements. This would apply not only in neutrino physics but also in hadron collider measurements.

7.4.1 Determination of the F_3 Structure Function and GLS Sum Rule

For quantitative studies of inclusive deep-inelastic lepton-nucleon scattering, it is vital to have precise measurements of the F_3 structure functions as input into global PDF fits. Because it depends on weak axial quark charges, the F_3 structure function can only be measured with neutrino and antineutrino beams and is unique in its ability to differentiate between the quark and antiquark content of the nucleon. On a proton target, for instance, the neutrino and antineutrino F_3 structure functions (at leading order in α_s) are given by

$$xF_3^{\nu p}(x) = 2x\left(d(x) - \overline{u}(x) + s(x) + \cdots\right), \quad (7.13)$$

$$xF_3^{\overline{\nu} p}(x) = 2x\left(u(x) - \overline{d}(x) - \overline{s}(x) + \cdots\right), \quad (7.14)$$

$$xF_3^{\nu n}(x) = 2x\left(u(x) - \overline{d}(x) + s(x) + \cdots\right), \quad (7.15)$$

$$xF_3^{\overline{\nu} n}(x) = 2x\left(d(x) - \overline{u}(x) - \overline{s}(x) + \cdots\right). \quad (7.16)$$

where $u_v = u - \bar{u}$ and $d_v = d - \bar{d}$ are the valence sea quark distributions. Under the assumption of a symmetric strange sea, i.e., $s(x) = \bar{s}(x)$, the above expressions show that a measurement of the average $xF_3 = (xF_3^{\nu N} + xF_3^{\bar{\nu} N})/2$ for neutrino and antineutrino interactions on isoscalar targets provides a direct determination of the valence quark distributions in the proton. This measurement is complementary to the measurement of Drell-Yan production at colliders, which is essentially proportional to the sea quark distributions.

The first step in the structure function analysis is the measurement of the differential cross section:

$$\frac{1}{E_\nu}\frac{d\sigma^2}{dxdQ^2} = \frac{N(x,Q^2,E_\nu)}{N(E_\nu)}\frac{\sigma_{\rm tot}/E_\nu}{dxdQ^2} \tag{7.17}$$

where $N(x,Q^2,E_\nu)$ is the number of events in each (x,Q^2,E_ν) bin and $N(E_\nu)$ is the number of events in each E_ν bin integrated over x and Q^2. The average xF_3 structure function can be extracted by taking the difference between neutrino and antineutrino differential cross sections:

$$\frac{1}{E_\nu}\frac{d^2\sigma^\nu}{dxdQ^2} - \frac{1}{E_\nu}\frac{d^2\sigma^{\bar\nu}}{dxdQ^2} = 2\left[y\left(1-\frac{y}{2}\right)\frac{y}{Q^2}\right]xF_3 \tag{7.18}$$

where xF_3 denotes the sum for neutrino and antineutrino interactions.

The determination of the xF_3 structure functions will, in turn, allow a precision measurement of the Gross-Llewellyn-Smith (GLS) QCD sum rule:

$$\begin{aligned} S_{\rm GLS}(Q^2) &= \frac{1}{2}\int_0^1 \frac{1}{x}\left[xF_3^{\nu N} + xF_3^{\bar\nu N}\right]dx \\ &= 3\left[1 - \frac{\alpha_s(Q^2)}{\pi} - a(n_f)\left(\frac{\alpha_s(Q^2)}{\pi}\right)^2 - b(n_f)\left(\frac{\alpha_s(Q^2)}{\pi}\right)^3\right] + \Delta\mathrm{HT} \end{aligned} \tag{7.19}$$

where α_s is the strong coupling constant, n_f is the number of quark flavors, a and b are known functions of n_f, and the quantity ΔHT represents higher-twist contributions. The equation above can be inverted to determine $\alpha_s(Q^2)$ from the GLS sum rule. The most precise determination of the GLS sum rule was obtained by the CCFR experiment on an iron target [43] $S_{\rm GLS}(Q^2 = 3\,GeV^2) = 2.50 \pm 0.018 \pm 0.078$. The high-resolution ND combined with the unprecedented statistics would substantially reduce the systematic uncertainty on the low-x extrapolation of the xF_3 structure functions entering the GLS integral. In addition, the presence of different nuclear targets, as well as the availability of a target with free protons will allow investigation of isovector and nuclear corrections, and adding a tool to test isospin (charge) symmetry (Section 7.5).

7.4.2 Determination of the Longitudinal Structure Function $F_L(x, Q^2)$

The structure function F_L is directly related to the gluon distribution $G(x,Q^2)$ of the nucleon, as can be seen from the Altarelli-Martinelli relation:

$$F_L(x,Q^2) = \frac{\alpha_s(Q^2)}{\pi}\left[\frac{4}{3}\int_x^1\frac{dy}{y}\left(\frac{x}{y}\right)^2 F_2(x,Q^2) + n_f\int_x^1\frac{dy}{y}\left(\frac{x}{y}\right)^2\left(1-\frac{x}{y}\right)G(y,Q^2)\right] \tag{7.20}$$

where n_f is the number of parton flavors. In the leading order approximation the longitudinal structure function F_L is zero, while at higher orders a nonzero $F_L(x,Q^2)$ is originated as a consequence of the violation of the Callan-Gross relation:

$$F_L(x,Q^2) = \left(1+\frac{4M^2x^2}{Q^2}\right)F_2(x,Q^2) - 2xF_1(x,Q^2) \tag{7.21}$$

where $2xF_1 = F_T$ is the transverse structure function. A measurement of $R = F_L/F_T$ is therefore both a test of perturbative QCD at large x and a clean probe of the gluon density at small x where the quark contribution is small. A poor knowledge of R, especially at small x, results in uncertainties in the structure functions extracted from deep inelastic scattering cross sections, and in turn, in electroweak measurements. It is instructive to compare the low-Q^2 behavior of R for charged-lepton versus neutrino scattering. In both cases CVC implies that $F_T \propto Q^2$ as $Q^2 \to 0$. However, while $F_L \propto Q^4$ for the electromagnetic current, for the weak current F_L is dominated by the finite PCAC (partial conservation of the axial current) contribution [26]. The behavior of R at $Q^2 \ll 1$ GeV^2 is therefore very different for charged-lepton and neutrino scattering. A new precision measurement of the Q^2 dependence of R with (anti)neutrino data would also clarify the size of the high-twist contributions to F_L and R, which reflect the strength of multi-parton correlations (qq and qg).

The ratio of longitudinal to transverse structure functions can be measured from the y dependence of the deep inelastic scattering data. Fits to the following function:

$$F(x, Q^2, \epsilon) = \frac{\pi(1-\epsilon)}{y^2 G_F^2 M E_\nu} \left[\frac{d^2\sigma^\nu}{dxdy} + \frac{d^2\sigma^{\bar{\nu}}}{dxdy}\right] = 2xF_1(x, Q^2)\left[1 + \epsilon R(x, Q^2)\right] \tag{7.22}$$

have been used by CCFR and NuTeV to determine $R = \sigma_L/\sigma_T$. In this equation $\epsilon \simeq 2(1-y)/(1+(1-y)^2)$ is the polarization of the virtual W boson. This equation assumes $xF_3^\nu = xF_3^{\bar{\nu}}$, and a correction must be applied if this is not the case. The values of R are extracted from linear fits to F versus ϵ at fixed x and Q^2 bins.

7.4.3 Determination of F_2^n and the d/u Ratio of Quark Distribution Functions

Because of the larger electric charge on the u quark than on the d, the electromagnetic proton F_2 structure function data provide strong constraints on the u-quark distribution, but are relatively insensitive to the d-quark distribution. To constrain the d-quark distribution a precise knowledge of the corresponding F_2^n structure functions of free neutrons is required, which in current practice is extracted from inclusive deuterium F_2 data. At large values of x ($x > 0.5$) the nuclear corrections in deuterium become large and, more importantly, strongly model-dependent, leading to large uncertainties on the resulting d-quark distribution. Using the isospin relation $F_2^{\bar{\nu}p} = F_2^{\nu n}$ and $F_2^{\nu p} = F_2^{\bar{\nu}n}$ it is possible to obtain a direct determination of $F_2^{\nu n}$ and $F_2^{\bar{\nu}n}$ with neutrino and antineutrino scattering off a target with free protons. This determination is free from model uncertainties related to nuclear targets. The extraction of $F_2^{\nu n}$ and $F_2^{\bar{\nu}n}$ will allow a precise extraction on the d-quark distribution at large x. Existing neutrino data on hydrogen have relatively large errors and do not extend beyond $x \sim 0.5$ [44,45].

The $F_2^{\bar{\nu}p}$ and $F_2^{\nu p}$ structure functions can be obtained from interactions on a target with free protons after subtracting the contributions from xF_3 and R. These latter can either be modeled within global PDF fits or taken from the other two measurements described above. As discussed in Section 7.5

the LBNE ND can achieve competitive measurements of $F_2^{\bar{\nu}p}$ and $F_2^{\nu p}$ with an increase of statistics of three orders of magnitude with respect to the existing hydrogen data [44,45].

7.4.4 Measurement of Nucleon Structure Functions

At present neutrino scattering measurements of cross sections have considerably larger uncertainties than those of the electromagnetic inclusive cross sections. The measurement of the differential cross sections [8] is dominated by three uncertainties: (1) muon energy scale, (2) hadron energy scale, and (3) knowledge of the input (anti)neutrino flux. Table 7.4 shows a comparison of past and present experiments and the corresponding uncertainties on the energy scales. The most precise measurements are from the CCFR, NuTeV and NOMAD experiments, which are limited to a statistics of about 10^6 neutrino events.

Table 7.4: Summary of past experiments performing structure function measurements. The expected numbers in the LBNE near detector for a five-year run with the 1.2-MW 120-GeV reference beam (5×10^{21} POT) are also given for comparison.

Experiment	Mass	ν_μ CC Stat.	Target	E_ν (GeV)	ΔE_μ	ΔE_{H}
CDHS [46]	750 t	10^7	p,Fe	20-200	2.0%	2.5%
BEBC [47,48]	various	5.7×10^4	p,D,Ne	10-200		
CCFR [49,50]	690 t	1.0×10^6	Fe	30-360	1.0%	1.0%
NuTeV [51]	690 t	1.3×10^6	Fe	30-360	0.7%	0.43%
CHORUS [52]	100 t	3.6×10^6	Pb	10-200	2.5%	5.0%
NOMAD [14]	2.7 t	1.3×10^6	C	5-200	0.2%	0.5%
[16]	18 t	1.2×10^7	Fe	5-200	0.2%	0.6%
MINOS ND [13]	980 t	3.6×10^6	Fe	3-50	2-4%	5.6%
LBNE ND	5 t	5.9×10^7	$(C_3H_6)_n$	0.5-30	$< 0.2\%$	$< 0.5\%$

The MINERνA [53] experiment is expected to provide new structure function measurements on a number of nuclear targets including He, C, Fe and Pb in the near future. Since the structure function measurement mainly involves DIS events, the MINERνA measurement will achieve a competitive statistics after the completion of the new run with the medium-energy beam. MINERνA will focus on a measurement of the ratio of different nuclear targets to measure nuclear corrections in (anti)neutrino interactions. It must be noted that the MINERνA experiment relies on the MINOS ND for muon identification. The corresponding uncertainty on the muon-energy scale (Table 7.4) is substantially larger than that in other modern experiments, e.g., NuTeV and NOMAD, thus limiting the potential of absolute structure function measurements. Furthermore, the muon-energy scale is also the dominant source of uncertainty in the determination of the (anti)neutrino fluxes with the low-ν method. Therefore, the flux uncertainties in MINERνA are expected to be larger than in NOMAD and NuTeV.

Given its reference beam design and 1.2-MW proton-beam power, LBNE expects to collect about 2.3×10^7 neutrino DIS events and about 4.4×10^6 antineutrino DIS events in the ND. These numbers correspond to an improvement by more than one order of magnitude with respect to the most precise past experiments, e.g., NuTeV [51] and NOMAD [14,16]. With these high-statistics samples, LBNE will be able to significantly reduce the gap between the uncertainties on the weak and electromagnetic structure functions. A possible high-energy run with the upgraded 2.3-MW beam would offer a further increase by more than a factor of ten in statistics.

In addition to the large data samples, the use of a high-resolution, low-density spectrometer allows LBNE to reduce systematic uncertainties with respect to previous measurements. The LBNE ND is expected to achieve precisions better than 0.2% and 0.5% on the muon- and hadron-energy scales, respectively. These numbers are based on the results achieved by the NOMAD experiment (Table 7.4), which had much lower statistics and poorer resolution than is expected in the LBNE ND. The calibration of the momentum and energy scales will be performed with the large sample of reconstructed $K^0_S \to \pi\pi$, $\Lambda \to p\pi$, and $\pi^0 \to \gamma\gamma$ decays. In addition, the overall hadronic energy scale can be calibrated by exploiting the well-known structure of the Bjorken y distribution in (anti)neutrino DIS interactions [14,54]. The relative fluxes as a function of energy can be extracted to a precision of about 2% with the low-ν method, due to the small uncertainty on the muon-energy scale. The world average absolute normalization of the differential cross sections $\sigma_{\rm tot}/E$, is known to 2.1% precision [55]. However, with the 1.2-MW beam available from the PIP-II upgrades, it will be possible to improve the absolute normalization using ν-e NC elastic scattering events, coherent meson production, etc. An overall precision of 1-2% would make (anti)neutrino measurements comparable to or better than the complementary measurements from charged-lepton DIS.

On the time scale of LBNE, comparable measurements from (anti)neutrino experiments are not expected, primarily due to the low energy of competing beamlines (J-PARC neutrino beamline in Japan [56]) or to the poorer resolution of the detectors used (MINERνA [53] , T2K [57], NOνA [58]). The experimental program most likely to compete with the LBNE ND measurements is the 12-GeV upgrade at Jefferson Laboratory (JLab) [59]. However, it must be emphasized that the use of electron beams at JLab makes this program *complementary* to LBNE's. In particular, the three topics discussed above are specific to the (anti)neutrino interactions.

Several planned experiments at JLab with the energy-upgraded 12-GeV beam will measure the d/u ratio from D targets up to $x \sim 0.85$, using different methods to minimize the nuclear corrections. The LBNE measurement will be competitive with the proposed JLab 12-GeV experiments, since the large statistics expected will allow a precise determination of $F_2^{\nu n}$ and $F_2^{\bar{\nu} n}$ up to $x \sim 0.85$. Furthermore, the use of a weak probe coupled with a wide-band beam will provide a broader Q^2 range than in JLab experiments, thus allowing a separation of higher twist and other sub-leading effects in $1/Q^2$.

7.5 Tests of Isospin Physics and Sum-Rules

One of the most compelling physics topics accessible to LBNE's high-resolution near detector is the isospin physics using neutrino and antineutrino interactions. This physics involves the Adler sum rule and tests isospin (charge) symmetry in nucleons and nuclei.

The Adler sum rule relates the integrated difference of the antineutrino and neutrino F_2 structure functions to the isospin of the target:

$$\mathcal{S}_A(Q^2) = \int_0^1 dx \, \left[F_2^{\overline{\nu}}(x,Q^2) - F_2^{\nu}(x,Q^2)\right]/(2x) = 2\, I_z, \tag{7.23}$$

where the integration is performed over the entire kinematic range of the Bjorken variable x and I_z is the projection of the target isospin vector on the quantization axis (z axis). For the proton $\mathcal{S}_A^p = 1$ and for the neutron $\mathcal{S}_A^n = -1$.

In the quark-parton model the Adler sum is the difference between the number of valence u and d quarks of the target. The Adler sum rule survives the strong-interaction effects because of the conserved vector current (CVC) and provides an exact relation to test the local current commutator algebra of the weak hadronic current. In the derivation of the Adler sum rule the effects of both non-conservation of the axial current and heavy-quark production are neglected.

Experimental tests of the Adler sum rule require the use of a hydrogen target to avoid nuclear corrections to the bound nucleons inside the nuclei. The structure functions $F_2^{\overline{\nu}}$ and F_2^{ν} have to be determined from the corresponding differential cross sections and must be extrapolated to small x values in order to evaluate the integral. The test performed in bubble chambers by the BEBC Collaboration — the only test available — is limited by the modest statistics; it used about 9,000 $\overline{\nu}$ and 5,000 ν events collected on hydrogen [48].

The LBNE program can provide the first high-precision test of the Adler sum rule. To this end, the use of the high-energy beam tune shown in Figure 3.19, although not essential, would increase the sensitivity, allowing attainment of higher Q^2 values. Since the use of a liquid H_2 bubble chamber is excluded in the ND hall due to safety concerns, the (anti)neutrino interactions off a hydrogen target can only be extracted with a subtraction method from the composite materials of the ND targets. Using this technique to determine the position resolution in the location of the primary vertex is crucial to reducing systematic uncertainties. For this reason, a precision test of the Adler sum rule is best performed with the low-density magnetized ND.

A combination of two different targets — the polypropylene $(C_3H_6)_n$ foils placed in front of the STT modules and pure carbon foils — are used in the low-density, magnetized ND to provide a fiducial hydrogen mass of about 1 t. With the LBNE fluxes from the standard exposure, $5.0(1.5) \times 10^6 \pm 13(6.6) \times 10^3 (sub.)$ $\nu(\overline{\nu})$ CC events (where the quoted uncertainty is dominated by the statistical subtraction procedure) would be collected on the hydrogen target. The level of precision that can be achieved is sufficient to open up the possibility of making new discoveries in the quark and hadron structure of the proton. No other comparable measurement is expected on the timescale of LBNE.

7.6 Studies of (Anti)Neutrino-Nucleus Interactions

An integral part of the physics program envisioned for the LBNE ND involves detailed measurements of (anti)neutrino interactions in a variety of nuclear targets. The LBNE ND offers substantially larger statistics coupled with a much higher resolution and, in turn, lower systematic uncertainties with respect to past experiments (Table 7.4) or ongoing and future ones (MINERνA [53], T2K [57], NOνA [58]). The most important nuclear target is of course the argon target, which matches the LBNE far detector. The ND standard target is polypropylene $(C_3H_6)_n$, largely provided by the mass of the STT radiators. An additional proposed ND target is argon gas in pressurized aluminum tubes with sufficient mass to provide $\simeq$10 times the ν_μCC and NC statistics as expected in the LBNE far detector. Equally important nuclear targets are carbon (graphite), which is essential in order to get (anti)neutrino interactions on free protons through a statistical subtraction procedure from the main polypropylene target (Section 7.5), and calcium. In particular, this latter target has the same atomic weight ($A = 40$) as argon but is isoscalar. One additional nuclear target is iron, which is used in the proposed India-based Neutrino Observatory (INO) [60]. The modularity of the STT provides for successive measurements using thin nuclear targets (thickness $< 0.1X_0$), while the excellent angular and space resolution allows a clean separation of events originating in different target materials. Placing an arrangement of different nuclear targets upstream of the detector provides the desired nuclear samples in (anti)neutrino interactions. For example, a single 7-mm-thick calcium layer at the upstream end of the detector will provide about 3.1×10^5 ν_μCC interactions in one year.

Potential ND studies in nuclear effects include the following:

- nuclear modifications of form factors
- nuclear modifications of structure functions
- mechanisms for nuclear effects in coherent and incoherent regimes
- a dependence of exclusive and semi-exclusive processes
- effect of final-state interactions
- effect of short-range correlations
- two-body currents

The study of nuclear effects in (anti)neutrino interactions off nuclei is directly relevant for the long-baseline oscillation studies. The use of heavy nuclei like argon in the LBNE far detector requires a measurement of nuclear cross sections on the same targets in the ND in order to reduce signal and background uncertainties in the oscillation analyses. Cross-section measurements obtained from other experiments using different nuclei are not optimal; in addition to the different p/n ratio in argon compared to iron or carbon where measurements from other experiments exist, nuclear modifications of cross sections can differ from 5% to 15% between carbon and argon for example, while the difference in the final-state interactions could be larger. Additionally, nuclear modifications can introduce a substantial smearing of the kinematic variables reconstructed from the observed final-state particles. Detailed measurements of the dependence on the atomic number A of different exclusive processes are then required in order to understand the absolute energy scale of neutrino event interactions and to reduce the corresponding systematic uncertainties on the oscillation parameters.

It is worth noting that the availability of a free-proton target through statistical subtraction of the $(C_3H_6)_n$ and carbon targets (Section 7.5) will allow for the first time a direct model-independent measurement of nuclear effects — including both the primary and final-state interactions — on the argon target relevant for the far detector oscillation analysis.

Furthermore, an important question in nuclear physics is how the structure of a nucleon is modified when said nucleon is inside the medium of a heavy nucleus as compared to a free nucleon like the proton in a hydrogen nucleus. Studies of the ratio of structure functions of nuclei to those of free nucleons (or in practice, the deuteron) reveal nontrivial deviations from unity as a function of x and Q^2. These have been well explored in charged-lepton scattering experiments, but little empirical information exists from neutrino scattering. Measurements of structure using neutrino scattering are complementary to those in charged-lepton scattering.

Another reason to investigate the nuclear-medium modifications of neutrino structure functions is that most neutrino scattering experiments are performed on nuclear targets, from which information on the free nucleon is inferred by performing a correction for the nuclear effects. In practice this often means applying the same nuclear correction as for the electromagnetic structure functions, which introduces an inherent model-dependence in the result. In particular, significant differences between photon-induced and weak-boson-induced nuclear structure functions are predicted, especially at low Q^2 and low x, which have not been tested. A striking example is offered by the ratio R of the longitudinal-to-transverse structure functions [26]. While the electromagnetic ratio tends to zero in the photoproduction limit, $Q^2 \to 0$, by current conservation, the ratio for neutrino structure functions is predicted to be *finite* in this limit. Thus, significant discovery potential exists in the study of neutrino scattering from nuclei.

The comparison of argon and calcium targets ($^{40}_{18}$Ar and $^{40}_{20}$Ca) in the LBNE ND would be particularly interesting. Since most nuclear effects depend on the atomic weight A, inclusive properties of (anti)neutrino interactions are expected to be the same for these two targets [26,61,62,63]. This fact would allow the use of both targets to model signal and backgrounds in the LBNE far detector (argon target), as well as to compare LBNE results for nuclear effects on argon with the extensive data on calcium from charged lepton DIS. In addition, a high-precision measurement of (anti)neutrino interactions in both argon and calcium opens the possibility for studying a potential flavor and isovector dependence of nuclear effects and to further test the isospin (charge symmetry) in nuclei (Section 7.5). Evidence for any of these effects would constitute important discoveries.

Finally, the extraction of (anti)neutrino interactions on deuterium from the statistical subtraction of H_2O from D_2O, which is required to measure the fluxes (Section 7.1), would allow the first direct measurement of nuclear effects in deuterium. This measurement can be achieved since the structure function of a free isoscalar nucleon is given by the average of neutrino and antineutrino structure functions on hydrogen ($F_2^{\nu n} = F_2^{\bar{\nu} p}$). A precise determination of nuclear modifications of structure functions in deuterium would play a crucial role in reducing systematic uncertainties from the global PDF fits.

7.7 Search for Heavy Neutrinos

The most economical way to handle the problems of neutrino masses, dark matter and the Baryon Asymmetry of the Universe in a unified way may be to add to the Standard Model (SM) three Majorana singlet fermions with masses roughly on the order of the masses of known quarks and leptons using the seesaw mechanism [64]. The appealing feature of this theory (called the νMSM for *Neutrino Minimal SM*) [65] is that every left-handed fermion has a right-handed counterpart, leading to a consistent way of treating quarks and leptons.

The most efficient mechanism proposed for producing these heavy sterile singlet states experimentally is through weak decays of heavy mesons and baryons, as can be seen from the left-hand diagram in Figure 7.4, showing some examples of relevant two- and three-body decays [66]. These heavy mesons can be produced by energetic protons scattering off the LBNE neutrino production target and the heavy singlet neutrinos from their decays detected in the near detector.

The lightest of the three new singlet fermions in the νMSM, is expected to have a mass from 1 keV to 50 keV [67] and could play the role of the dark matter particle [68]. The two other neutral fermions are responsible for giving mass to ordinary neutrinos via the seesaw mechanism at the *electroweak scale* and for creation of the Baryon Asymmetry of the Universe (BAU; for a review see [67]). The masses of these particles and their coupling to ordinary leptons are constrained by particle physics experiments and cosmology [66,69]. They should be almost degenerate, thus nearly forming Dirac fermions (this is dictated by the requirement of successful baryogenesis). Different considerations indicate that their mass should be in the region of $\mathcal{O}(1)$ GeV [70]. The mixing

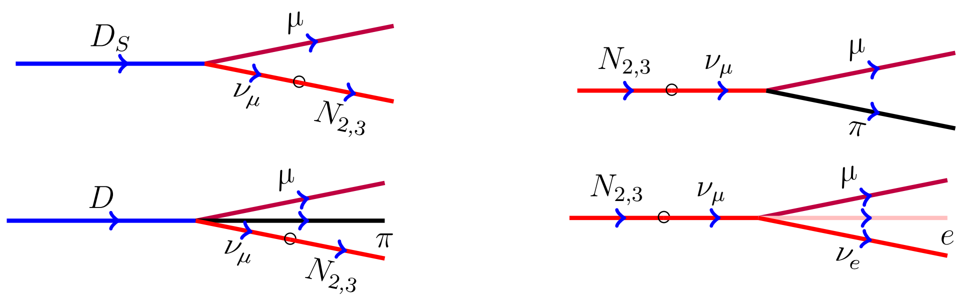

Figure 7.4: Left: Feynman diagrams of meson decays producing heavy sterile neutrinos. Right: Feynman diagrams of sterile-neutrino decays.

angle, U^2, between the singlet fermions and the three active-neutrino states must be small [65,71] — otherwise the large mixing would have led to equilibration of these particles in the early Universe above the electroweak temperatures, and, therefore, to erasing of the BAU — explaining why these new particles have not been seen previously.

Several experiments have conducted searches for heavy neutrinos, for example BEBC [72], CHARM [73], NuTeV [74] and the CERN PS191 experiment [75,76] (see also a discussion of different experiments in [69]). In the search for heavy neutrinos, the strength of the LBNE ND, compared to earlier experiments, lies in reconstructing the exclusive decay modes, including electronic, hadronic and muonic. Furthermore, the detector offers a means to constrain and measure the backgrounds using control samples.

In case of the LBNE experiment the relevant heavy mesons are charmed. With a typical lifetime (in the rest frame) of about 10^{-10} s, these mesons mostly decay before further interaction, yielding the sterile-neutrino flux. Since these sterile neutrinos are very weakly interacting they can cover quite a large distance before decay, significantly exceeding the distance of roughly 500 m from the target to the ND. The ND can search for decays of neutrinos into SM particles due to mixing with active neutrinos, provided a sufficiently long instrumented decay region is available. Two examples of the interesting decay modes are presented on the right panel of Figure 7.4. More examples can be found in [66].

An estimate of sterile-neutrino events that can be observed in the LBNE ND, N^{LBNE}_{signal}, is obtained by comparing the relevant parameters of the LBNE and CHARM experiments. The number of events grows linearly with the number of protons on target, the number of produced charmed mesons, the detector length (decay region) and the detector area. In particular, this latter linear increase is valid if the angular spread of the neutrino flux, which is on the order of $N_m M_D/E_{beam}$, is larger than the angle at which the ND is seen from the target. Here N_m is the multiplicity of the produced hadrons, and the above condition is valid for both LBNE and CHARM. The number of events decreases linearly when the energy increases, since this increases the lifetime, reducing the decay probability within the detector. Finally, the number of mesons decreases quadratically with the distance between the target and the detector.

The considerations above imply that a search for νMSM sterile neutrinos in the LBNE ND can be competitive after only five years of running with the reference beam, corresponding to an overall integrated exposure of about 5×10^{21} POT with a proton energy of 120 GeV. The use of a low-density, high-resolution spectrometer in the ND substantially reduces backgrounds and allows the detection of both leptonic and hadronic decay modes. Assuming a fiducial length of the magnetized tracker of 7 m as decay region, the ratio between the signal event to be observed in the LBNE ND and those in the CHARM experiment can be estimated to be more than a factor of 50 after only four years of running. Since both production and decay rates are proportional to the square of the neutrino mixing angles, the corresponding improvement in the square of the neutrino mixing angle U^2 will be about a factor of seven with respect to the CHARM experiment. Figure 7.5 shows the projected LBNE sensitivity in the (U^2, M) plane. At lower values of the mass of the heavy neutrinos, additional constraints can be obtained for kaons by comparing the LBNE and PS191 experiments, as shown in Figure 7.5.

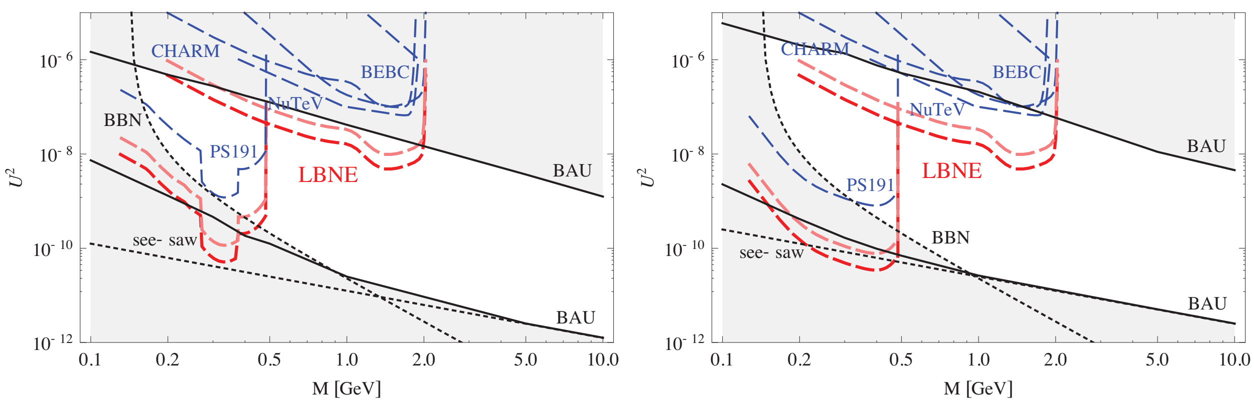

Figure 7.5: Upper limits on U^2, the mixing angle between heavy sterile neutrinos and the light active states, coming from the Baryon Asymmetry of the Universe (solid lines), from the seesaw mechanism (dotted line) and from the Big Bang nucleosynthesis (dotted line). The regions corresponding to different experimental searches are outlined by blue dashed lines. Left panel: normal hierarchy; right panel: inverted hierarchy (adopted from [77]). Pink and red curves indicate the expected sensitivity of the LBNE near detector with an exposure of 5×10^{21} POT (~ 5 years) with the 1.2-MW reference beam at 120 GeV for detector lengths of 7 m and 30 m , respectively (see text for details).

It must be noted that exploitation of the complete 5 + 5 years ($\nu + \overline{\nu}$) years of data taking would further improve the number of expected events by a factor of two, since it scales linearly with the number of protons on target. With the beam upgrade to 2.3-MW, this improvement would become a factor of four with respect to the initial five year run and the 1.2 MW beam.

A better sensitivity to νMSM can be achieved by instrumenting the upstream region of the ND hall (e.g., with the liquid argon detector and some minimal tracking device upstream). The fiducial volume of the new detector will need to be empty (material-free) or fully sensitive in order to suppress background events. The geometry of the ND hall would allow a maximal decay length of about 30 m. The sensitivity of this configuration can be estimated by rescaling the expected limits on the neutrino mixing angle U^2. The expected number of signal events with a total decay length of $\sim$ 30 m exceeds by about 200 (800) times the number of events in CHARM after a five (5 +5) year run with the standard (upgraded) beam. In turn, this implies an improvement by a factor of 15 (28) in the sensitivity to U^2 with respect to the CHARM experiment.

If the magnetic moment of the sterile neutrinos is sizeable, the dominant decay channel would be a radiative electromagnetic decay into $\gamma\nu$, which has also been proposed as a possible explanation for the observed MiniBooNE low-energy excess [78]. This possibility, in turn, requires a detector capable of identifying and reconstructing single photon events. The low-density ND in LBNE can achieve an excellent sensitivity to this type of search as demonstrated by a similar analysis in NOMAD [79].

7.8 Search for High Δm^2 Neutrino Oscillations

The evidence for neutrino oscillations obtained from atmospheric, long-baseline accelerator, solar and long-baseline reactor data from different experiments consistently indicates two different scales, with Δm^2_{32} $\sim$2.4 $\times$ 10^{-3} eV^2 defining the atmospheric oscillations (also long-baseline accelerator and short-baseline reactor scales) and Δm^2_{21} $\sim$7.9 $\times$ 10^{-5} eV^2 defining the solar oscillations (and long-baseline reactor oscillations). The only way to accommodate oscillations with relatively high Δm^2 at the eV^2 scale as suggested by the results from the LSND experiment [80] is therefore to add one or more sterile neutrinos to the conventional three light neutrinos.

Recently, the MiniBooNE experiment reported that its antineutrino data might be consistent with the LSND $\overline{\nu}_\mu \rightarrow \overline{\nu}_e$ oscillation with $\Delta m^2 \sim$ eV^2 [81]. Contrary to the antineutrino data, the neutrino data seem to exclude high Δm^2 oscillations, possibly indicating a different behavior between neutrinos and antineutrinos.

Models with five (3+2) or six (3+3) neutrinos can potentially explain the MiniBooNE results. In addition to the cluster of the three neutrino mass states (accounting for *solar* and *atmospheric* mass splitting), two (or three) states at the eV scale are added, with a small admixture of ν_e and ν_μ to account for the LSND signal. One distinct prediction from such models is a significant probability for $\overline{\nu}_\mu$ disappearance into sterile neutrinos, on the order of 10%, in addition to the small probability for $\overline{\nu}_e$ appearance.

Given a roughly 500-m baseline and a low-energy beam, the LBNE ND can reach the same value $L/E_\nu \sim 1$ as MiniBooNE and LSND. The large fluxes and the availability of fine-grained detectors make the LBNE program well suited to search for active-sterile neutrino oscillations beyond the three-flavor model with Δm^2 at the eV^2 scale.

Due to the potential differences between neutrinos and antineutrinos, four possibilities have to be considered in the analysis: ν_μ disappearance, $\overline{\nu}_\mu$ disappearance, ν_e appearance and $\overline{\nu}_e$ appearance. As discussed in Section 7.1, the search for high Δm^2 oscillations has to be performed simultaneously with the in situ determination of the fluxes.

To this end, an independent prediction of the ν_e and $\overline{\nu}_e$ fluxes starting from the measured ν_μ and $\overline{\nu}_\mu$ CC distributions are required since the ν_e and $\overline{\nu}_e$ CC distributions could be distorted by the appearance signal. The low-ν_0 method can provide such predictions if external measurements for the K^0_L component are available from hadro-production experiments (Section 7.1).

The study will implement an iterative procedure:

1. extraction of the fluxes from ν_μ and $\overline{\nu}_\mu$ CC distributions assuming no oscillations are present
2. comparison with data and determination of oscillation parameters (if any)
3. new flux extraction after subtraction of the oscillation effect
4. iteration until convergence

The analysis has to be performed separately for neutrinos and antineutrinos due to potential CP or CPT violation, according to MiniBooNE/LSND data. The ratio of ν_e CC events to ν_μ CC events will be measured:

$$\mathcal{R}_{e\mu}(L/E) \equiv \frac{\#\ of\ \nu_e N \to e^- X}{\#\ of\ \nu_\mu N \to \mu^- X}(L/E); \qquad \overline{\mathcal{R}}_{e\mu}(L/E) \equiv \frac{\#\ of\ \overline{\nu}_e N \to e^+ X}{\#\ of\ \overline{\nu}_\mu N \to \mu^+ X}(L/E) \quad (7.24)$$

This is then compared with the predictions obtained from the low-ν_0 method. Deviations of $\mathcal{R}_{e\mu}$ or $\overline{\mathcal{R}}_{e\mu}$ from the expectations as a function of L/E would provide evidence for oscillations. This procedure only provides a relative measurement of $\nu_e(\overline{\nu}_e)$ versus $\nu_\mu(\overline{\nu}_\mu)$; since the fluxes are extracted from the observed ν_μ and $\overline{\nu}_\mu$ CC distributions, an analysis of the $\mathcal{R}_{e\mu}(\overline{\mathcal{R}}_{e\mu})$ ratio cannot distinguish between $\nu_\mu(\overline{\nu}_\mu)$ disappearance and $\nu_e(\overline{\nu}_e)$ appearance.

The process of NC elastic scattering off protons (Section 7.3) can provide the complementary measurement needed to disentangle the two hypotheses of $\nu_\mu(\overline{\nu}_\mu)$ disappearance into sterile neutrinos and $\nu_e(\overline{\nu}_e)$ appearance. In order to cancel systematic uncertainties, the NC/CC ratio with respect to QE scattering will be measured:

$$\mathcal{R}_{NC}(L/E) \equiv \frac{\#\ of\ \nu p \to \nu p}{\#\ of\ \nu_\mu n \to \mu^- p}(L/E); \qquad \overline{\mathcal{R}}_{NC}(L/E) \equiv \frac{\#\ of\ \overline{\nu} p \to \overline{\nu} p}{\#\ of\ \overline{\nu}_\mu p \to \mu^+ n}(L/E) \quad (7.25)$$

It is possible to reconstruct the neutrino energy from the proton angle and momentum under the assumption that the nuclear smearing effects are small enough to neglect (the same for the neutrino CC sample). In the oscillation analysis, only the *relative* distortions of the ratio $\mathcal{R}_{NC}(\overline{\mathcal{R}}_{NC})$ as a function of L/E are of interest, not their absolute values. For $Q^2 > 0.2$ GeV^2 the relative shape of the total cross sections is not very sensitive to the details of the form factors. To improve the energy resolution, it is possible to use neutrino interaction events originating from the deuterium inside the D_2O target embedded into the fine-grained tracker. These events have better energy resolution due to the smaller nuclear smearing effects in D_2O.

An improved oscillation analysis is based on a simultaneous fit to both $\mathcal{R}_{e\mu}(\overline{\mathcal{R}}_{e\mu})$ and $\mathcal{R}_{NC}(\overline{\mathcal{R}}_{NC})$. The first ratio provides a measurement of the oscillation parameters while the latter constrains the $\nu_e(\overline{\nu}_e)$ appearance versus the $\nu_\mu(\overline{\nu}_\mu)$ disappearance. This analysis imposes two main requirements on the ND:

- e^+/e^- separation to provide an unambiguous check of the different behavior between neutrinos and antineutrinos suggested by MiniBooNE
- accurate reconstruction of proton momentum and angle

Validation of the unfolding of the high Δm^2 oscillations from the in situ extraction of the $\nu(\overline{\nu})$ flux would also require changes to the beam conditions, since the ND cannot be easily moved. This would require a short run with a high-energy beam and the capability to change or switch off the beam focusing system.

7.9 Light (sub-GeV) Dark Matter Searches

According to the latest cosmological and astrophysical measurements, nearly eighty percent of the matter in the Universe is in the form of cold, non-baryonic dark matter (DM) [82,83]. The search to find evidence of the particle (or particles) that make up DM, however, has so far turned up empty. Direct detection experiments and indirect measurements at the LHC, however, are starting to severely constrain the parameter space of Weakly-Interacting Massive Particles (WIMPs), one of the leading candidates for DM. The lack of evidence for WIMPs at these experiments has forced many in the theory community to reconsider.

Some theories consider an alternative possibility to the WIMP paradigm in which the DM mass is much lighter than the electroweak scale (e.g., below the GeV level). In order to satisfy constraints on the relic density of DM, these theories require that DM particles be accompanied by light *mediator* particles that would have allowed for efficient DM annihilation in the early Universe. In the simplest form of these theories an extra U(1) gauge field mixes with the SM U(1) gauge field, but with an additional kinetic term. This mixing term provides a *portal* from the dark sector to the charged particles of the SM. In this model, the mediators are called *dark photons* and are denoted by V.

Recently, a great deal of interest has been paid to the possibility of studying models of light (sub-GeV) Dark Matter at low-energy, fixed-target experiments [84,85,86,87]. High-flux neutrino beam experiments — such as LBNE — have been shown to potentially provide coverage of DM+mediator parameter space that cannot be covered by either direct detection or collider experiments.

Upon striking the target, the proton beam can produce the dark photons either directly through $pp(pn) \to V$ as in the left-hand diagram of Figure 7.6 or indirectly through the production of a π^0 or a η meson which then promptly decays into a SM photon and a dark photon as in the center diagram in the figure. For the case where $m_V > 2m_{DM}$, the dark photons will quickly decay into a pair of DM particles.

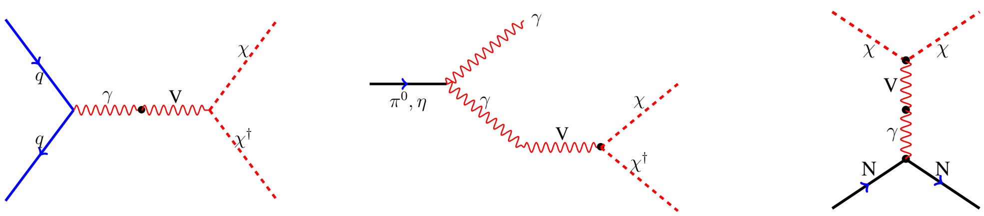

Figure 7.6: On the left is shown the direct production of a dark photon, while, in the center, the dark photon is produced via the decay of a neutral pion or eta meson. In both cases, the dark photon promptly decays into a pair of DM particles. Right: Tree-level scattering of a DM particle off of nuclei. Analogous interactions with electrons in the detector are also possible.

The LBNE ND together with the high-intensity beam will provide an excellent setup for making this measurement. The relativistic DM particles from the beam will travel along with the neutrinos to the detector where they can be detected through NC-like interactions either with electrons or nucleons, as shown in the right-hand diagram of Figure 7.6. Since the signature of a DM event looks similar to that of a neutrino event, the neutrino beam provides the major source of background for the DM signal.

Several ways have been proposed to suppress neutrino backgrounds using the unique characteristics of the DM beam. Since DM will travel much more slowly than the much lighter neutrinos, DM events in the ND will arrive out of time with the beam pulse. In addition, since the electrons struck by DM will be in a much more forward direction compared to neutrino interactions, the angle of these electrons may be used to reduce backgrounds, taking advantage of the ND's fine angular resolution.

Finally, a special run can be devised to turn off the focusing horn to significantly reduce the charged particle flux that will produce neutrinos. Figure 7.7 shows the expected sensitivity of the MiniBooNE DM search using this technique [87]. With a wider-band, higher-energy, more intense

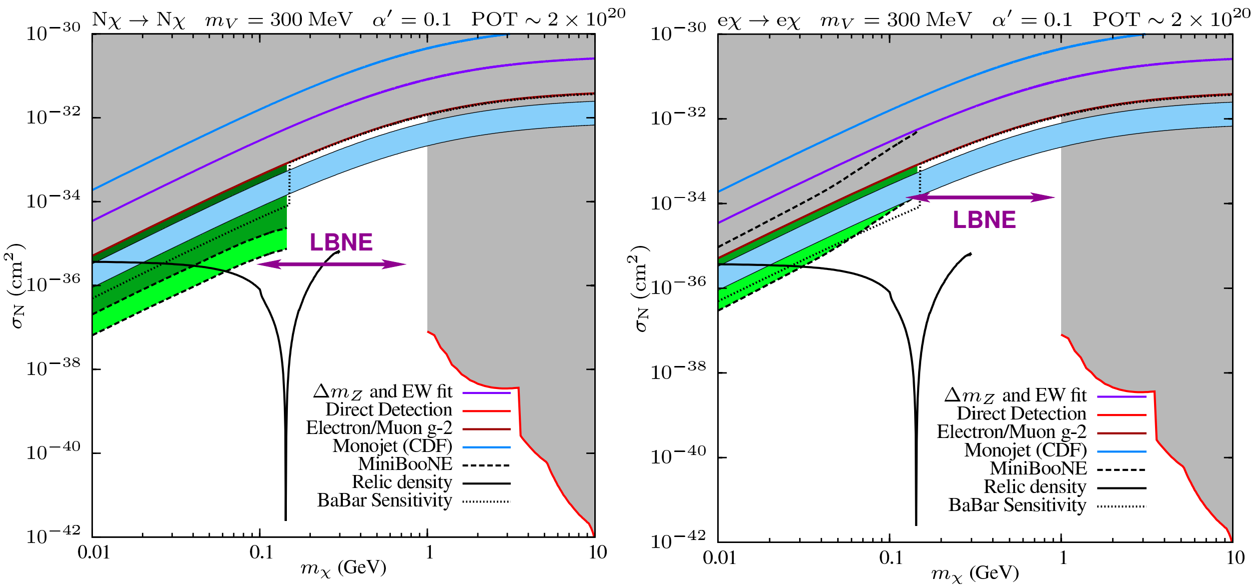

Figure 7.7: Regions of nucleon-WIMP scattering cross section (corresponding to dark matter in the lab moving with $v = 10^{-3}c$). The plot uses $m_V = 300$ MeV and $\alpha' = 0.1$. Constraints are shown from different experiments. The left plot shows the exclusion regions expected from MiniBooNE given 1-10 (light green), 10-1000 (green), and more than 1000 (dark green) elastic scattering events off nucleons. The right panel shows the same for elastic scattering off electrons. The magenta arrows indicate the region where LBNE can extend the MiniBooNE sensitivity. Figure is based on studies in [87].

beam, LBNE is expected to not only cover the MiniBooNE sensitivity region with higher statistics, but will also extend the sensitivity to cover the region between MiniBooNE and the direct DM searches. If the LBNE ND were a LArTPC and the entire detector volume active, the effective number of DM events detected would be much higher when compared to a MINOS-like detector of the same mass. Much more thorough studies must be conducted to obtain reliable sensitivities. This requires an integration of theoretical predictions into a simulation package for the detector.

References

1. B. Choudhary *et al.*, **Indian Institutions and Fermilab Collaboration** , "LBNE-India Detailed Project Report (DPR) submitted to DAE, India," `LBNE-doc-6704`, 2012. Cited in Section 7 (pg.163).
2. D. Casper, "The Nuance neutrino physics simulation, and the future," *Nucl.Phys.Proc.Suppl.* **112** (2002) 161–170, `arXiv:hep-ph/0208030 [hep-ph]`.
3. G. Zeller, "Nuclear Effects in Water vs. Argon," `LBNE-doc-740`, 2010.
4. G. Zeller, "Expected Event Rates in the LBNE Near Detector," `LBNE-doc-783`, 2010.
5. S.R.Mishra, Apr, 1990. Review talk presented at Workshop on Hadron Structure Functions and Parton Distributions, Fermilab. Cited in Section 7.1.1 (pg.164).
6. R. Raja, "The Main injector particle production experiment (MIPP) at Fermilab," *Nucl.Instrum.Meth.* **A553** (2005) 225–230, `arXiv:hep-ex/0501005 [hep-ex]`. Cited in Section 7.1.2 (pg.166).
7. A. Korzenev, **NA61/SHINE** , "Hadron production measurement from NA61/SHINE," `arXiv:1311.5719 [nucl-ex]`, 2013. Cited in Section 7.1.2 (pg.166).
8. J. Formaggio and G. Zeller, "From eV to EeV: Neutrino Cross Sections Across Energy Scales," *Rev.Mod.Phys.* **84** (2012) 1307, `arXiv:1305.7513 [hep-ex]`. Cited in Sections 7.1.3 (pg.166) and 7.4.4 (pg.182).
9. W. J. Marciano and Z. Parsa, "Neutrino-Electron Scattering Theory," *J. Phys.* **G29** (2003) 2629–2645, `arXiv:hep-ph/0403168`. Cited in Sections 7.1.4 (pg.167) and 7.2.2 (pg.173).
10. S. Mishra, K. Bachmann, R. Bernstein, R. Blair, C. Foudas, *et al.*, "Measurement of Inverse Muon Decay $\nu_\mu + e \to \mu^- + \nu_e$ at Fermilab Tevatron Energies 15-GeV - 600-GeV," *Phys.Rev.Lett.* **63** (1989) 132–135. Cited in Section 7.1.5 (pg.167).
11. S. Mishra, K. Bachmann, R. Blair, C. Foudas, B. King, *et al.*, "Inverse Muon Decay, $\nu_\mu e \to \mu^- \nu_e$, at the Fermilab Tevatron," *Phys.Lett.* **B252** (1990) 170–176. Cited in Section 7.1.5 (pg.167).
12. P. Vilain *et al.*, **CHARM-II Collaboration** , "A Precise measurement of the cross-section of the inverse muon decay muon-neutrino + e- –> mu- + electron-neutrino," *Phys.Lett.* **B364** (1995) 121–126. Cited in Section 7.1.5 (pg.167).
13. P. Adamson *et al.*, **MINOS Collaboration** , "Neutrino and Antineutrino Inclusive Charged-current Cross Section Measurements with the MINOS Near Detector," *Phys.Rev.* **D81** (2010) 072002, `arXiv:0910.2201 [hep-ex]`. Cited in Section 7.1.8 (pg.169).
14. Q. Wu *et al.*, **NOMAD Collaboration** , "A Precise measurement of the muon neutrino-nucleon inclusive charged current cross-section off an isoscalar target in the energy range 2.5 < E(nu) < 40-GeV by NOMAD," *Phys.Lett.* **B660** (2008) 19–25, `arXiv:0711.1183 [hep-ex]`. Cited in Sections 7.1.8 (pg.169) and 7.4.4 (pg.183).

15. V. Lyubushkin *et al.*, **NOMAD Collaboration** , "A Study of quasi-elastic muon neutrino and antineutrino scattering in the NOMAD experiment," *Eur.Phys.J.* **C63** (2009) 355–381, `arXiv:0812.4543 [hep-ex]`. Cited in Section 7.1.8 (pg.169).
16. O. Samoylov *et al.*, **NOMAD** , "A Precision Measurement of Charm Dimuon Production in Neutrino Interactions from the NOMAD Experiment," *Nucl.Phys.* **B876** (2013) 339–375, `arXiv:1308.4750 [hep-ex]`. Cited in Sections 7.1.8 (pg.169), 7.2.1 (pg.172), and 7.4.4 (pg.183).
17. G. Zeller *et al.*, **NuTeV Collaboration** , "A Precise determination of electroweak parameters in neutrino nucleon scattering," *Phys.Rev.Lett.* **88** (2002) 091802, `arXiv:hep-ex/0110059 [hep-ex]`. Cited in Section 7.2.1 (pg.170).
18. H. Abramowicz, R. Belusevic, A. Blondel, H. Blumer, P. Bockmann, *et al.*, **CDHS Collaboration** , "A Precision Measurement of sin**2theta(W) from Semileptonic Neutrino Scattering," *Phys.Rev.Lett.* **57** (1986) 298. Cited in Section 7.2.1 (pg.171).
19. J. Allaby *et al.*, **CHARM Collaboration** , "A Precise Determination of the Electroweak Mixing Angle from Semileptonic Neutrino Scattering," *Z.Phys.* **C36** (1987) 611. Cited in Section 7.2.1 (pg.171).
20. P. Reutens, F. Merritt, D. MacFarlane, R. Messner, D. Novikoff, *et al.*, **CCFR Collaboration** , "Measurement of $\sin^2\theta_W$ and ρ in Deep Inelastic Neutrino - Nucleon Scattering," *Phys.Lett.* **B152** (1985) 404–410. Cited in Section 7.2.1 (pg.171).
21. S. Alekhin, S. A. Kulagin, and R. Petti, "Modeling lepton-nucleon inelastic scattering from high to low momentum transfer," *AIP Conf.Proc.* **967** (2007) 215–224, `arXiv:0710.0124 [hep-ph]`. Cited in Section 7.2.1 (pg.172).
22. S. Alekhin, S. A. Kulagin, and R. Petti, "Update of the global fit of PDFs including the low-Q DIS data," `arXiv:0810.4893 [hep-ph]`, 2008. Cited in Section 7.2.1 (pg.172).
23. S. Alekhin, S. A. Kulagin, and R. Petti, "Determination of Strange Sea Distributions from Neutrino-Nucleon Deep Inelastic Scattering," *Phys.Lett.* **B675** (2009) 433–440, `arXiv:0812.4448 [hep-ph]`. Cited in Section 7.2.1 (pg.172).
24. A. Arbuzov, D. Y. Bardin, and L. Kalinovskaya, "Radiative corrections to neutrino deep inelastic scattering revisited," *JHEP* **0506** (2005) 078, `arXiv:hep-ph/0407203 [hep-ph]`. Cited in Section 7.2.1 (pg.172).
25. S. A. Kulagin and R. Petti, "Global study of nuclear structure functions," *Nucl.Phys.* **A765** (2006) 126–187, `arXiv:hep-ph/0412425 [hep-ph]`. Cited in Section 7.2.1 (pg.172).
26. S. A. Kulagin and R. Petti, "Neutrino inelastic scattering off nuclei," *Phys.Rev.* **D76** (2007) 094023, `arXiv:hep-ph/0703033 [HEP-PH]`. Cited in Sections 7.2.1 (pg.172), 7.4.2 (pg.181), and 7.6 (pg.186).
27. S. Kulagin and R. Petti, "Structure functions for light nuclei," *Phys.Rev.* **C82** (2010) 054614, `arXiv:1004.3062 [hep-ph]`. Cited in Section 7.2.1 (pg.172).
28. P. Vilain *et al.*, **CHARM-II Collaboration** , "Precision measurement of electroweak parameters from the scattering of muon-neutrinos on electrons," *Phys.Lett.* **B335** (1994) 246–252. Cited in Section 7.2.2 (pg.173).

29. A. Czarnecki and W. J. Marciano, "Polarized Moller scattering asymmetries," *Int.J.Mod.Phys.* **A15** (2000) 2365–2376, arXiv:hep-ph/0003049 [hep-ph].
30. S. Bennett and C. Wieman, "Erratum: Measurement of the 6s –> 7s Transition Polarizability in Atomic Cesium and an Improved Test of the Standard Model [Phys. Rev. Lett. 82, 2484 (1999)]," *Phys.Rev.Lett.* **82** (1999) 4153–4153.
31. W. Yao *et al.*, **Particle Data Group** , "Review of Particle Physics," *J.Phys.* **G33** (2006) 1–1232.
32. P. Anthony *et al.*, **SLAC E158 Collaboration** , "Precision measurement of the weak mixing angle in Moller scattering," *Phys.Rev.Lett.* **95** (2005) 081601, arXiv:hep-ex/0504049 [hep-ex].
33. J. H. Lee, "The Qweak: Precision measurement of the proton's weak charge by parity violating experiment," *Few Body Syst.* **54** (2013) 129–134. Cited in Section 7.2.2 (pg.175).
34. Nuruzzaman, "Q-weak: First Direct Measurement of the Weak Charge of the Proton," arXiv:1312.6009 [nucl-ex], 2013. Cited in Section 7.2.2 (pg.175).
35. R. Jaffe and A. Manohar, "The G(1) Problem: Fact and Fantasy on the Spin of the Proton," *Nucl.Phys.* **B337** (1990) 509–546. Cited in Section 7.3 (pg.175).
36. R. D. Young, J. Roche, R. D. Carlini, and A. W. Thomas, "Extracting nucleon strange and anapole form factors from world data," *Phys.Rev.Lett.* **97** (2006) 102002, arXiv:nucl-ex/0604010 [nucl-ex]. Cited in Sections 7.3.1 (pg.175) and 7.3.1 (pg.176).
37. D. B. Leinweber, S. Boinepalli, I. Cloet, A. W. Thomas, A. G. Williams, *et al.*, "Precise determination of the strangeness magnetic moment of the nucleon," *Phys.Rev.Lett.* **94** (2005) 212001, arXiv:hep-lat/0406002 [hep-lat]. Cited in Section 7.3.1 (pg.175).
38. L. Ahrens, S. Aronson, P. Connolly, B. Gibbard, M. Murtagh, *et al.*, "Measurement of Neutrino - Proton and anti-neutrino - Proton Elastic Scattering," *Phys.Rev.* **D35** (1987) 785. Cited in Section 7.3.2 (pg.177).
39. G. Garvey, W. Louis, and D. White, "Determination of proton strange form-factors from neutrino p elastic scattering," *Phys.Rev.* **C48** (1993) 761–765. Cited in Section 7.3.2 (pg.177).
40. W. Alberico, M. Barbaro, S. M. Bilenky, J. Caballero, C. Giunti, *et al.*, "Strange form-factors of the proton: A New analysis of the neutrino (anti-neutrino) data of the BNL-734 experiment," *Nucl.Phys.* **A651** (1999) 277–286, arXiv:hep-ph/9812388 [hep-ph]. Cited in Section 7.3.2 (pg.177).
41. A. Aguilar-Arevalo *et al.*, **MiniBooNE Collaboration** , "Measurement of the Neutrino Neutral-Current Elastic Differential Cross Section on Mineral Oil at $E_\nu \sim 1$ GeV," *Phys.Rev.* **D82** (2010) 092005, arXiv:1007.4730 [hep-ex]. Cited in Section 7.3.2 (pg.177).
42. L. Bugel *et al.*, **FINeSSE Collaboration** , "A Proposal for a near detector experiment on the booster neutrino beamline: FINeSSE: Fermilab intense neutrino scattering scintillator experiment," FERMILAB-PROPOSAL-0937, arXiv:hep-ex/0402007 [hep-ex], 2004. Cited in Section 7.3.2 (pg.178).

43. W. Leung, P. Quintas, S. Mishra, F. Sciulli, C. Arroyo, *et al.*, "A Measurement of the Gross-Llewellyn-Smith sum rule from the CCFR x(F3) structure function," *Phys.Lett.* **B317** (1993) 655–659. Cited in Section 7.4.1 (pg.180).
44. A. Bodek and A. Simon, "What Do Electron and Neutrino Experiments Tell Us About Nuclear Effects in the Deuteron," *Z.Phys.* **C29** (1985) 231. Cited in Sections 7.4.3 (pg.181) and 7.4.3 (pg.182).
45. G. Jones *et al.*, **Birmingham-CERN-Imperial Coll.-MPI(Munich)-Oxford-University Coll. Collaboration** , "A Measurement of the Proton Structure Functions From Neutrino Hydrogen and Anti-neutrino Hydrogen Charged Current Interactions," *Z.Phys.* **C44** (1989) 379–384. Cited in Sections 7.4.3 (pg.181) and 7.4.3 (pg.182).
46. J. Berge, H. Burkhardt, F. Dydak, R. Hagelberg, M. Krasny, *et al.*, "A Measurement of Differential Cross-Sections and Nucleon Structure Functions in Charged Current Neutrino Interactions on Iron," *Z.Phys.* **C49** (1991) 187–224.
47. D. Allasia *et al.*, **WA25 Collaboration** , "Measurement of the Neutron and Proton Structure Functions From Neutrino and Anti-neutrinos Scattering in Deuterium," *Phys.Lett.* **B135** (1984) 231.
48. D. Allasia, C. Angelini, A. Baldini, L. Bertanza, A. Bigi, *et al.*, "Q**2 Dependence of the Proton and Neutron Structure Functions from Neutrino and anti-neutrinos Scattering in Deuterium," *Z.Phys.* **C28** (1985) 321. Cited in Section 7.5 (pg.184).
49. U.-K. Yang *et al.*, **CCFR/NuTeV Collaboration** , "Measurements of F_2 and $xF_3^{\nu} - xF_3^{\bar{\nu}}$ from CCFR ν_μ–Fe and $\bar{\nu}_\mu$–Fe data in a physics model independent way," *Phys.Rev.Lett.* **86** (2001) 2742–2745, `arXiv:hep-ex/0009041 [hep-ex]`.
50. U.-K. Yang *et al.*, **CCFR/NuTeV Collaboration** , "Extraction of R = sigma(L) / sigma(T) from CCFR Fe-neutrino(muon) and Fe-anti-neutrino(muon) differential cross-sections," *Phys.Rev.Lett.* **87** (2001) 251802, `arXiv:hep-ex/0104040 [hep-ex]`.
51. M. Tzanov *et al.*, **NuTeV Collaboration** , "Precise measurement of neutrino and anti-neutrino differential cross sections," *Phys.Rev.* **D74** (2006) 012008, `arXiv:hep-ex/0509010 [hep-ex]`. Cited in Section 7.4.4 (pg.183).
52. G. Onengut *et al.*, **CHORUS Collaboration** , "Measurement of nucleon structure functions in neutrino scattering," *Phys.Lett.* **B632** (2006) 65–75.
53. B. Osmanov, **MINERvA Collaboration** , "MINERvA Detector: Description and Performance," `arXiv:1109.2855 [physics.ins-det]`, 2011. Cited in Sections 7.4.4 (pg.182), 7.4.4 (pg.183), and 7.6 (pg.185).
54. R. Petti and O. Samoylov, "Charm dimuon production in neutrino-nucleon interactions in the NOMAD experiment," *Phys.Part.Nucl.Lett.* **8** (2011) 755–761. Cited in Section 7.4.4 (pg.183).
55. J. Beringer *et al.*, **Particle Data Group** , "Review of Particle Physics (RPP)," *Phys.Rev.* **D86** (2012) 010001. Cited in Section 7.4.4 (pg.183).
56. T. Sekiguchi, "Neutrino facility and neutrino physics in J-PARC," *PTEP* **2012** (2012) 02B005. Cited in Section 7.4.4 (pg.183).

57. K. Abe *et al.*, **T2K Collaboration** , "The T2K Experiment," *Nucl.Instrum.Meth.* **A659** (2011) 106–135, `arXiv:1106.1238 [physics.ins-det]`. Cited in Sections 7.4.4 (pg.183) and 7.6 (pg.185).
58. D. Ayres *et al.*, **NOvA Collaboration** , "The NOvA Technical Design Report," FERMILAB-DESIGN-2007-01, 2007. `http://lss.fnal.gov/archive/design/fermilab-design-2007-01.pdf`. Cited in Sections 7.4.4 (pg.183) and 7.6 (pg.185).
59. J. Dudek, R. Ent, R. Essig, K. Kumar, C. Meyer, *et al.*, "Physics Opportunities with the 12 GeV Upgrade at Jefferson Lab," *Eur.Phys.J.* **A48** (2012) 187, `arXiv:1208.1244 [hep-ex]`. Cited in Section 7.4.4 (pg.183).
60. N. Mondal, "India-Based Neutrino Observatory (INO)," *Eur.Phys.J.Plus* **127** (2012) 106. Cited in Section 7.6 (pg.185).
61. A. Butkevich, "Quasi-elastic neutrino charged-current scattering off medium-heavy nuclei: 40Ca and 40Ar," *Phys.Rev.* **C85** (2012) 065501, `arXiv:1204.3160 [nucl-th]`. Cited in Section 7.6 (pg.186).
62. A. Butkevich and S. A. Kulagin, "Quasi-elastic neutrino charged-current scattering cross sections on oxygen," *Phys.Rev.* **C76** (2007) 045502, `arXiv:0705.1051 [nucl-th]`. Cited in Section 7.6 (pg.186).
63. A. M. Ankowski and J. T. Sobczyk, "Construction of spectral functions for medium-mass nuclei," *Phys.Rev.* **C77** (2008) 044311, `arXiv:0711.2031 [nucl-th]`. Cited in Section 7.6 (pg.186).
64. T. Yanagida, "Horizontal Symmetry and Masses of Neutrinos," *Prog.Theor.Phys.* **64** (1980) 1103. Cited in Section 7.7 (pg.187).
65. T. Asaka and M. Shaposhnikov, "The nuMSM, dark matter and baryon asymmetry of the universe," *Phys.Lett.* **B620** (2005) 17–26, `arXiv:hep-ph/0505013 [hep-ph]`. Cited in Sections 7.7 (pg.187) and 7.7 (pg.188).
66. D. Gorbunov and M. Shaposhnikov, "How to find neutral leptons of the νMSM?," *JHEP* **0710** (2007) 015, `arXiv:0705.1729 [hep-ph]`. Cited in Sections 7.7 (pg.187) and 7.7 (pg.188).
67. A. Boyarsky, O. Ruchayskiy, and M. Shaposhnikov, "The Role of sterile neutrinos in cosmology and astrophysics," *Ann.Rev.Nucl.Part.Sci.* **59** (2009) 191–214, `arXiv:0901.0011 [hep-ph]`. Cited in Section 7.7 (pg.187).
68. S. Dodelson and L. M. Widrow, "Sterile-neutrinos as dark matter," *Phys.Rev.Lett.* **72** (1994) 17–20, `arXiv:hep-ph/9303287 [hep-ph]`. Cited in Section 7.7 (pg.187).
69. A. Atre, T. Han, S. Pascoli, and B. Zhang, "The Search for Heavy Majorana Neutrinos," *JHEP* **0905** (2009) 030, `arXiv:0901.3589 [hep-ph]`. Cited in Sections 7.7 (pg.187) and 7.7 (pg.188).
70. M. Shaposhnikov, "The nuMSM, leptonic asymmetries, and properties of singlet fermions," *JHEP* **0808** (2008) 008, `arXiv:0804.4542 [hep-ph]`. Cited in Section 7.7 (pg.187).

71. E. K. Akhmedov, V. Rubakov, and A. Y. Smirnov, "Baryogenesis via neutrino oscillations," *Phys.Rev.Lett.* **81** (1998) 1359–1362, `arXiv:hep-ph/9803255 [hep-ph]`. Cited in Section 7.7 (pg.188).
72. A. M. Cooper-Sarkar *et al.*, **WA66 Collaboration** , "Search for Heavy Neutrino Decays in the BEBC Beam Dump Experiment," *Phys.Lett.* **B160** (1985) 207. Cited in Section 7.7 (pg.188).
73. F. Bergsma *et al.*, **CHARM Collaboration** , "A Search for Decays of Heavy Neutrinos in the Mass Range 0.5-GeV to 2.8-GeV," *Phys.Lett.* **B166** (1986) 473. Cited in Section 7.7 (pg.188).
74. A. Vaitaitis *et al.*, **NuTeV Collaboration, E815 Collaboration** , "Search for Neutral Heavy Leptons in a High-Energy Neutrino Beam," *Phys.Rev.Lett.* **83** (1999) 4943–4946, `arXiv:hep-ex/9908011 [hep-ex]`. Cited in Section 7.7 (pg.188).
75. G. Bernardi, G. Carugno, J. Chauveau, F. Dicarlo, M. Dris, *et al.*, "Search for Neutrino Decay," *Phys.Lett.* **B166** (1986) 479. Cited in Section 7.7 (pg.188).
76. G. Bernardi, G. Carugno, J. Chauveau, F. Dicarlo, M. Dris, *et al.*, "Further Limits on Heavy Neutrino Couplings," *Phys.Lett.* **B203** (1988) 332. Cited in Section 7.7 (pg.188).
77. L. Canetti and M. Shaposhnikov, "Baryon Asymmetry of the Universe in the NuMSM," *JCAP* **1009** (2010) 001, `arXiv:1006.0133 [hep-ph]`.
78. A. Aguilar-Arevalo *et al.*, **MiniBooNE Collaboration** , "Unexplained Excess of Electron-Like Events From a 1-GeV Neutrino Beam," *Phys.Rev.Lett.* **102** (2009) 101802, `arXiv:0812.2243 [hep-ex]`. Cited in Section 7.7 (pg.190).
79. C. Kullenberg *et al.*, **NOMAD Collaboration** , "A Search for Single Photon Events in Neutrino Interactions in NOMAD," *Phys.Lett.* **B706** (2012) 268–275, `arXiv:1111.3713 [hep-ex]`. Cited in Section 7.7 (pg.190).
80. C. Volpe, N. Auerbach, G. Colo, T. Suzuki, and N. Van Giai, "Neutrino C-12 reactions and the LSND and KARMEN experiments on neutrino oscillations," *Phys. Atom. Nucl.* **64** (2001) 1165–1168. Cited in Section 7.8 (pg.190).
81. M. Maltoni and T. Schwetz, "Sterile neutrino oscillations after first MiniBooNE results," *Phys.Rev.* **D76** (2007) 093005, `arXiv:0705.0107 [hep-ph]`. Cited in Section 7.8 (pg.190).
82. P. Ade *et al.*, **Planck Collaboration** , "Planck 2013 results. XVI. Cosmological parameters," `arXiv:1303.5076 [astro-ph.CO]`, 2013. Cited in Section 7.9 (pg.192).
83. C. Bennett *et al.*, **WMAP** , "Nine-Year Wilkinson Microwave Anisotropy Probe (WMAP) Observations: Final Maps and Results," *Astrophys.J.Suppl.* **208** (2013) 20, `arXiv:1212.5225 [astro-ph.CO]`. Cited in Section 7.9 (pg.192).
84. B. Batell, M. Pospelov, and A. Ritz, "Exploring Portals to a Hidden Sector Through Fixed Targets," *Phys.Rev.* **D80** (2009) 095024, `arXiv:0906.5614 [hep-ph]`. Cited in Section 7.9 (pg.193).
85. P. deNiverville, M. Pospelov, and A. Ritz, "Observing a light dark matter beam with neutrino experiments," *Phys.Rev.* **D84** (2011) 075020, `arXiv:1107.4580 [hep-ph]`. Cited in Section 7.9 (pg.193).

86. P. deNiverville, D. McKeen, and A. Ritz, "Signatures of sub-GeV dark matter beams at neutrino experiments," *Phys.Rev.* **D86** (2012) 035022, arXiv:1205.3499 [hep-ph]. Cited in Section 7.9 (pg.193).
87. R. Dharmapalan *et al.*, **MiniBooNE Collaboration** , "Low Mass WIMP Searches with a Neutrino Experiment: A Proposal for Further MiniBooNE Running," FERMILAB-PROPOSAL-1032, arXiv:1211.2258 [hep-ex], 2012. Cited in Section 7.9 (pg.193).